Article

Meteorological OSSEs for new Zenith Total Delay observations: impact assessment for the Hydroterra geosynchronous satellite on the October 2019 Genoa event

Martina Lagasio [1], Agostino N. Meroni [2,1], Giorgio Boni [3], Luca Pulvirenti [1], Andrea Monti-Guarnieri [4], Roger Haagmans [5], Stephen Hobbs [6] and Antonio Parodi[1]*

[1] CIMA Research Foundation, Savona, 17100, Italy; martina.lagasio@cimafoundation.org (M.L.); luca.pulvirenti@cimafoundation.org (L.P.); agostino.meroni@cimafoundation.org (A.N.M.)
[2] Department of Civil and Environmental Engineering, Politecnico di Milano, Milan, 20133, Italy;
[3] Department of Civil, Chemical and Environmental Engineering, University of Genoa, Genoa, 16145, Italy; giorgio.boni@unige.it (G.B.)
[4] Department of Electronics, Information and Bioengineering, Politecnico di Milano, Milan, 20133 Italy; andrea.montiguarnieri@polimi.it (A.M.-G.)
[5] ESA - European Space Agency, Keplerlaan 1, 2201 AZ Noordwijk, The Netherlands; Roger.Haagmans@esa.int (R.A.)
[6] School of Aerospace, Transport and Manufacturing, Cranfield University, Bedford MK43 0AL, U.K.; S.E.Hobbs@cranfield.ac.uk (S.H.)
* Correspondence: antonio.parodi@cimafoundation.org; Tel.: +39-3489194083 (A.P.)

Version November 16, 2020 submitted to Remote Sens.

Abstract: Along the Mediterranean coastlines intense and localized rainfall events are responsible for numerous casualties and several million euros of damage every year. Numerical forecasts of such events are rarely skillful, because they lack information in their initial and boundary conditions at the relevant spatio-temporal scales, namely O(km) and O(h). In this context, the tropospheric delay observations (strongly related to the vertically integrated water vapor content) of the future geosynchronous Hydroterra satellite could provide valuable information at high spatio-temporal resolution. In this work, Observing System Simulation Experiments (OSSEs) are performed to assess the impact of assimilating this new observation in a cloud-resolving meteorological model, at different grid spacing and temporal frequency, and with respect to other existent observations. It is found that assimilating the Hydroterra observations at 2.5 km spacing every 3 or 6 hours has the largest positive impact on the forecast of the event under study. In particular, a better spatial localization and extent of the heavy rainfall area is achieved and a realistic surface wind structure, which is a crucial element in the forecast of such heavy rainfall events, is modelled.

Keywords: Mediterranean, extreme rainfall, geosynchronous satellite, InSAR, ZTD, IWV, data assimilation

1. Introduction

The Mediterranean region is frequently struck by severe rainfall events causing numerous casualties and several million euros of damage every year [1]. In particular, the unusually complex terrain of the western Mediterranean areas, characterized by high mountains close to the coastlines (Alps, Apennines, Massif Central, Pyrenees), can enhance or trigger the deep convective processes often originating over the warm sea in the fall season [2–4]. Among the heaviest rainfall phenomena of this region, there are Mesoscale Convective Systems (MCSs). On short time-scales, their relevance is due to their high probability of triggering floods and flash-floods, with significant societal impacts, often combined with numerous shortcomings in their forecast [5–7]. Being characterised by very high accumulated rainfall depths, they are also responsible for a large proportion of rainfall on annual time-scales. Climate projections suggest that their importance, in terms of frequency and intensity, is likely to increase in a warming climate. Recent studies demonstrate a strong sensitivity of the predicted climate impacts to the numerical representation of MCSs, with current climate models not generally capturing MCSs well enough [8]. Thus, improving the forecast accuracy of MCSs is a fundamental step towards managing their social and economic damage on both the short and the long term.

The advance of Numerical Weather Prediction (NWP) models to increasingly higher grid spacing (km and sub-km) is paving the way to potential new synergies with space-borne systems. On the one hand, to drive high resolution NWP models, high resolution input data and boundary conditions are needed. On the other hand, the present state-of-the-art high resolution NWP models coincides with the increasing availability of space-borne observational data sources characterized either by high spatial resolution (e.g. the Sentinel missions developed in the Copernicus program framework) or by high temporal resolution (Global Navigation Satellite System, GNSS).

In this context, the Synthetic Aperture Radar (SAR) Interferometry (InSAR) technique [9–12] applied to Sentinel-1 data enables the retrieval of information on a wide range of spatial scales of the potentially highly turbulent atmospheric water vapour field [13–18]. Many studies demonstrate the positive impact of assimilating Integrated Water Vapor (IWV) (measured in kg m^{-2}) or, equivalently, Zenith Total Delay (ZTD) [m] observations in the forecast of heavy rain, both from InSAR [19–23], and from GNSS [22,24–27]. Hence, it is expected that feeding NWP models with EO (Earth Observation) data-derived ZTD maps combining high spatial resolution and short revisit time can represent a breakthrough in the ability to forecast extreme weather events. However, nowadays, such space-borne observations with concurrently high spatial and temporal resolution are not available yet. On the one hand, Sentinel-1 ZTD maps have very high spatial resolution [28,29] but a too low temporal one, of the order of some days. On the other hand, GNSS ZTD timeseries are point measurements characterized by a coarser resolution (on the order of 30 km at best, much less in some regions) but they reach a temporal resolution of 30 s [22].

In the future, InSAR data at high temporal resolution (daily, or sub-daily) could be provided by geosynchronous satellites. The geosynchronous C-band SAR mission called Hydroterra is currently a phase 0 candidate mission for the 10^{th} Earth Explorer Programme of the European Space Agency (ESA). Hydroterra aims to observe the key processes of the daily water cycle by supplying frequent images (e.g., 1-12 h repeat time) at 1-3 km resolution. The geosynchronous orbit is expected to cover Europe and Africa. One of its main scientific objectives is to improve the physical insight and therefore the predictive capability of heavy rainfall and its possible consequences (floods, landslides) by providing estimates of ZTD, as well as of soil moisture, flood extent and presence of melting snow [30].

Concerning soil moisture, the added value of Hydroterra-derived estimates has been discussed in Cenci *et al.* [31]. To the best of our knowledge a similar kind of analysis has never been carried out for ZTD estimates from Hydroterra observations and their impacts on the predictive capability of severe hydro-meteorological events. In this work, to assess the added value of high resolution/high frequency ZTD estimates using future Hydroterra observations, a set of Observing System Simulation Experiments (OSSEs) is built. An OSSE is a numerical experiment conducted with a numerical prediction model (in this case a NWP model) and a data assimilation system that ingest simulated rather than real observations. Thus, a simulated scenario is used as reference instead of real-world observations, as explained in section 3. The OSSE approach is widely used to estimate the impacts of proposed designs of new satellites or new kinds of observations [32,33]. However, this is the first time that an OSSE is used to evaluate the potential of the Hydroterra data for NWP applications. In particular, the OSSEs are used both to understand the best way to assimilate this new kind of observation with the state-of-the-art data assimilation systems and to assess the most useful spatio-temporal resolution for NWP applications [34–38].

The aim of this work is twofold. Firstly, the sensitivity to different spatio-temporal resolutions of this new kind of ZTD observation is assessed to identify the best-performing setup in the simulation of a heavy rainfall event. Secondly, the added value of assimilating the Hydroterra-like ZTD field is compared to the forecasting skills of some experiments where already existing ZTD observations are assimilated, namely mimicking the GNSS Italian network coverage. Beyond a traditional and an object-based validation of the rainfall forecasts, the OSSEs results are also investigated using some physical criteria that are relevant for operational activities. Despite the OSSEs not being performed in fully operational configurations, this assures the relevance of the assimilation of the Hydroterra product to operational activities.

The work is organised as follows. In section 2, the use case is presented. Section 3 introduces the OSSE setup, a comparison between the reference run (to be used to produce the synthetic observations) and the experiment with no data assimilation, the observations to be assimilated, the assimilation techniques, the experiments, and the validation method. Results are presented in section **??**. Section 5 is devoted to the discussion and the interpretation of the results, while the conclusions are given in section 6.

2. Case study description

2.1. Study area

The study area, corresponding to the territory of the Italian region called Liguria, is located along the north-western coast of Italy (see Figure 1). From the morphological point of view, the region is characterized by high mountain ranges, with a maximum height between 1000 and 2000 m a.s.l. (above sea level) that run parallel to the coast and reach their maximum height a few kilometers from the coast. The particular morphology leads to the formation of meteorological patterns specific to the region, capable of producing rainfall of relatively short duration and extremely high intensity (up to an average of 200 mm in one hour and 500-600 mm in 12 hours) (see e.g. [39]). The particular meteorological situation, combined with the morphology, characterized by small basins with a high average slope, makes the region particularly exposed to flash flood risk. This type of morphology is very similar to that of several areas of the Mediterranean (e.g. Spanish, Greek, Algerian, French and Turkish coasts) as well as the hydro-meteorological events that cause economic damage and deaths [40–42]. The region provides an excellent study area representative of the entire Mediterranean belt subject to flash floods.

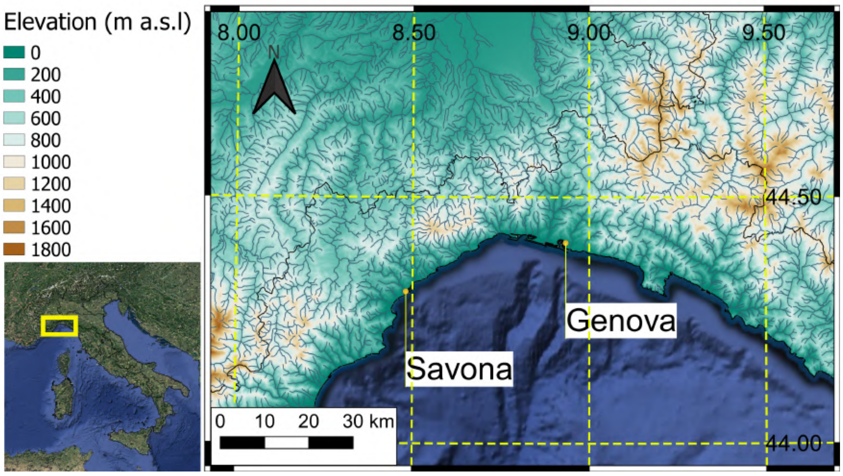

Figure 1. Study Area with orography and hydrography.

2.2. *Case study description*

The OSSEs are performed for a high impact weather event characterised by low predictability that occurred in Italy over the Liguria region between the 14^{th} and the 15^{th} of October 2019. The selected case study corresponds to a back-building MCS; these are among the most important flash-flood producing storms in the Liguria region area [2,4,43] and other Mediterranean coastal regions, such as southern France [3,44] and eastern Spain [45,46]. MCSs are known to have been common in these areas also in the past [47] and there is evidence that climate change could increase their frequency [48]. It is also known that their dynamics generally develop over the sea [44,49], which can control the rainfall intensity by modifying the atmospheric stability according to the average value of sea surface temperature [50–52], and can influence the low-level wind field by means of the differential thermal forcing due to sea surface temperature gradients [53,54]. The low predictability of this kind of event [4,55,56] is due to the fact that small-scale meteorological processes drive their dynamical evolutioy fiori17, for example, highlight the role of the convergence line that forms over the sea when a cold and dry continental air mass coming from inland meets a warm and wet maritime air mass. The cold air mass acts as a virtual orographic barrier that lifts the unstable warm air and triggers convection.

In addition to the mesoscale lifting, the other known ingredients for the development of a back-building MCS are a relatively high level of moisture, the presence of a conditionally unstable air mass, and slowly-evolving synoptic conditions [44].

On the 14^{th} of October 2019 a surface low pressure system located off the south-western coast of Ireland was associated with an upper-level trough extending as far south as the north African coasts, as shown in Figure 2(A). At that time, a cold front was approaching the Spanish coasts and a southerly low-level flow was developing off the Ligurian coasts (not shown). Similar conditions characterised the 15^{th} of October, see Figure 2(B), where the upper level divergence of the synoptic trough was placed over the Ligurian coasts and the moist and unstable flow kept blowing from the Mediterranean Sea. Such conditions are typical of the heavy rainfall events that are known to hit northern Italy in the Autumn [57–59]. As outlined before, these slow-evolving synoptic conditions are necessary for the MCS development but need to be accompanied by other local forcing factors (conditional instability, low-level moisture and mesoscale lifting), which significantly challenge the predictive capabilities of current NWP modelling tools.

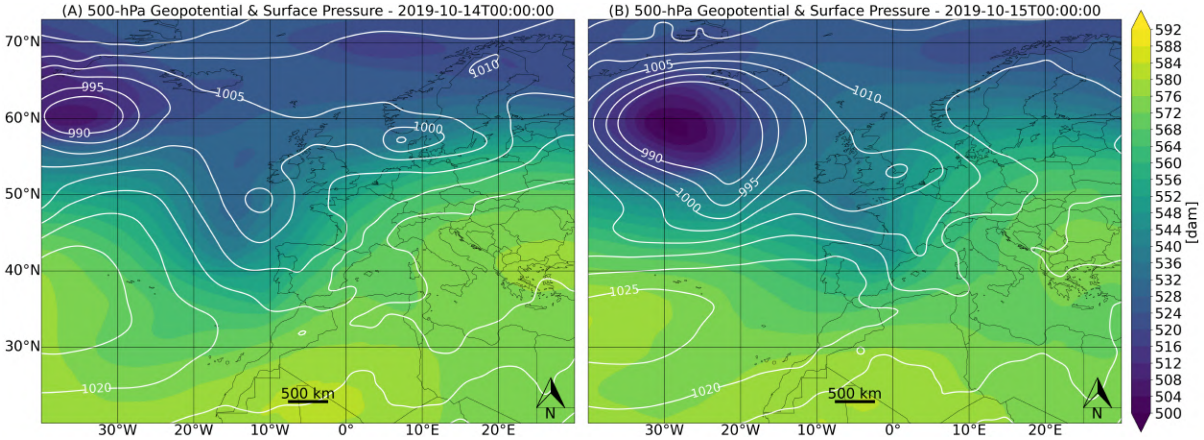

Figure 2. Sea level pressure (white contours, hPa) and 500 hPa geopotential height (colors, dam) on the 14th of October 2019 00UTC (A) and on the 15th of October 2019 00UTC (B). Data from ERA5 [60].

3. Methods and experiments

The underlying hypothesis of this study is that by assimilating high resolution ZTD maps, the NWP model can improve its spatial representation of the low-level moisture and the conditional instability. For the event under consideration, this can affect the local dynamics, possibly helping the development of a convergence line, which can act as a lifting factor for the triggering of the back-building MCS.

3.1. OSSE setup

The OSSEs setup is built following key points from Hoffman and Atlas [34] to guarantee its validity. The state-of-the-art Weather Research and Forecasting model [61, WRF, v3.8.1] is used to produce both the truth run (TR hereafter) and the forecast runs (FC hereafter), characterised by the following features:

- the TR and FC simulations are performed at different grid spacing using 3 two-way nested domains: 13.5, 4.5 and 1.5 km for TR (Figure 3A) and 22.5, 7.5 and 2.5 km for FC (Figure 3B). Both FC and TR have 50 vertical levels and all domains top reach 50 hPa;
- the TR is initialised at 00UTC of the 14th of October 2019 with the ECMWF-IFS (European Centre for Medium-Range Weather Forecasts Integrated Forecasting System) global model at 0.125° grid spacing and forced at the boundaries at an hourly frequency with the same product. The FC simulations are initialised at 00UTC of the 14th of October 2019 with the NCEP-GFS (National Centers for Environmental Prediction Global Forecast System) analysis and forecast data available at a horizontal grid spacing of $0.25° \times 0.25°$ and forced at the boundaries every three hours;
- the microphysical parameterizations used in the two use cases are the Aerosol-aware Thompson scheme for the TR [62] and the WSM6 (WRF Single Moment six-class) scheme for the FC simulations [63];
- the Digital Elevation Model (DEM) used in the numerical simulations is smoother in the FC setup than in the TR one: the WRF default filter has been applied 24 times for the TR and 36 for the FC.

The choice to use a higher resolution for the TR is mainly dictated by three considerations. Firstly, we needed to represent the phenomena under study with a sufficiently high resolution in the TR. Secondly, we wanted to have a TR ZTD field at a resolution which was as close as possible to the maximum resolution planned for the Hydroterra observations (on the order of 1 km) [64]. Thirdly, we aimed to evaluate the impact of the assimilation in a model with a setup currently used for operational forecasting activities. The remaining parameterizations (listed below) are the same for the TR and the FC experiments and follow the setup adopted in recent research [22,65,66]. They are also used in the setup implemented for operational forecast at CIMA Research Foundation[1] and include the Yonsei University scheme [67] for the planetary boundary layer turbulence closure; the RRTMG shortwave and longwave schemes [68–70] for radiation; the Rapid Update Cycle (RUC) scheme for the land surface model [71,72]. No cumulus scheme is activated in the two innermost domains (of both TR and FC runs), because the grid spacing is fine enough to explicitly resolve convection. An appropriate convective scheme, consistent with the boundary condition product, is activated in the outermost domain of both configurations: the Tiedke scheme [73,74] in the TR, and the new simplified Arakawa-Schubert scheme [75] in the FC experiments.

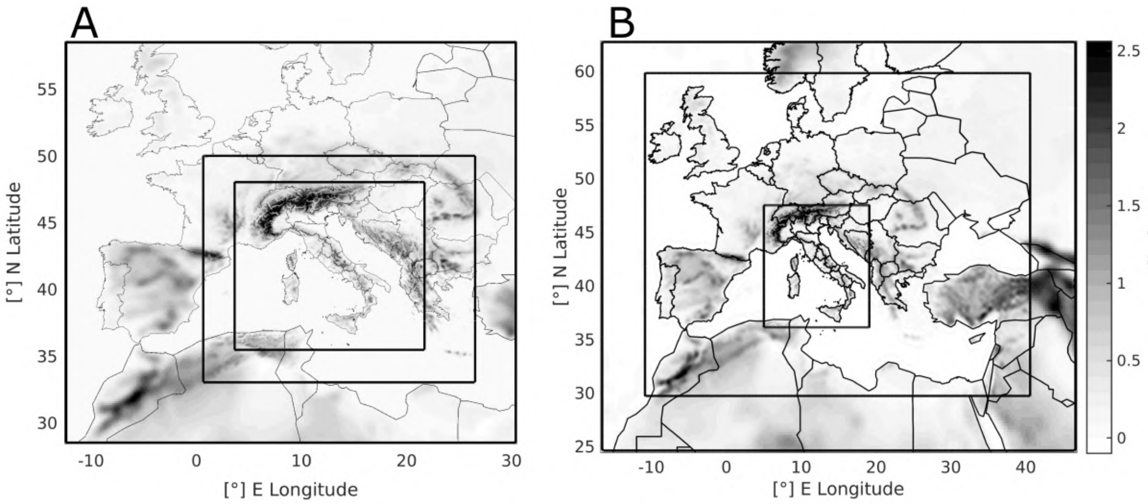

Figure 3. (A) TR setup: three two-way nested domains with 13.5, 4.5 and 1.5 km grid spacing. (B) FC setup: three two-way nested domains with 22.5, 7.5 and 2.5 km. Grey shading indicates the model terrein.

3.2. Comparison between TR and FC Open Loop

To assess the impact of ZTD assimilation at different spatial and temporal resolutions it is necessary that the TR differs significantly from the FC_OL (the FC Open Loop simulation, i.e. with no data assimilation) and, conversely, that it represents the rainfall field well enough.

In the TR, a back-building MCS is simulated, producing accumulated rainfall depths higher than 300 mm in 12 hours (Figure 4B). The simulation is very close to the back-building MCS accumulated rainfall observed by the merged radar and rain-gauges product (Figure 4A). As introduced in the previous subsection, MCSs are generally triggered by a strong and persistent (in time) convergence line over the sea, which fixes the generation of convective cells at the same position for a few hours, so that very high values of accumulated rainfall are produced [4,65,76]. Such a convergence line is visible during the main phase of the event (00, 01, 02 UTC) in the TR, as shown in Figure 5A-C.

Conversely, the FC_OL is not able to capture the correct dynamics of this event: Figure 5D-F shows that the convergence line is completely absent in the FC_OL simulation between 00 and 02 UTC. Consequently, the peak accumulated rainfall in 12 hours is less than 100 mm and the precipitation is more spatially distributed (Figure 4C). The dynamics of the TR and the FC_OL seem to significantly diverge in the afternoon of the 14th of October. In fact, in the morning of the 14th both configurations model a convergence line over the sea. Later during the day, in the FC_OL this line moves towards France and gets weaker, while in the TR the convergence line intensifies (not shown). This is likely due to either a wrong description of the thermodynamical state of the continental air mass in the FC_OL, which prevents it to overcome the orographic barrier and flow over the sea, or a too strong south-easterly flow from the sea, or a combination of both.

[1] www.cimafoundation.org/foundations/research-development/wrf.html

A correct representation of the convergence line in the NWP model has both dynamical and thermodynamical consequences. In fact, other than possibly producing vertical motion, the surface convergence line is also characterized by an anomalous water vapor content. This happens because the relatively dry continental air mass acts as a barrier for the moister maritime air mass [4], resulting in an accumulation of water vapor, which affects the air column stability. This is visible in Figure 5, where the 252 mm isoline of ZTD is shown in magenta. In fact, it is possible to see that, corresponding to the convergence line over the sea, a well defined finger-like structure of high water vapour content is modelled perpendicular to the Ligurian coast in the TR (Panels A, B, C). This area of relatively high humidity, in the first place, acts as source of water for the intense heavy rain, which is one of the necessary ingredients for the development of such phenomena [44]. Secondly, the higher humidity content in the TR, decreases the atmospheric stability. In fact, over the Ligurian Sea, the maximum Convective Available Potential Energy (mCAPE) is significantly higher in the TR, $O(2000 \text{ J kg}^{-1})$, than in the FC_OL, $O(1500 \text{ J kg}^{-1})$, as discussed in section 5 . Since in the FC_OL the convergence line is not produced, also the area of higher humidity is completely absent, with the consequences for the accumulated rainfall field discussed above (Panels D, E, F).

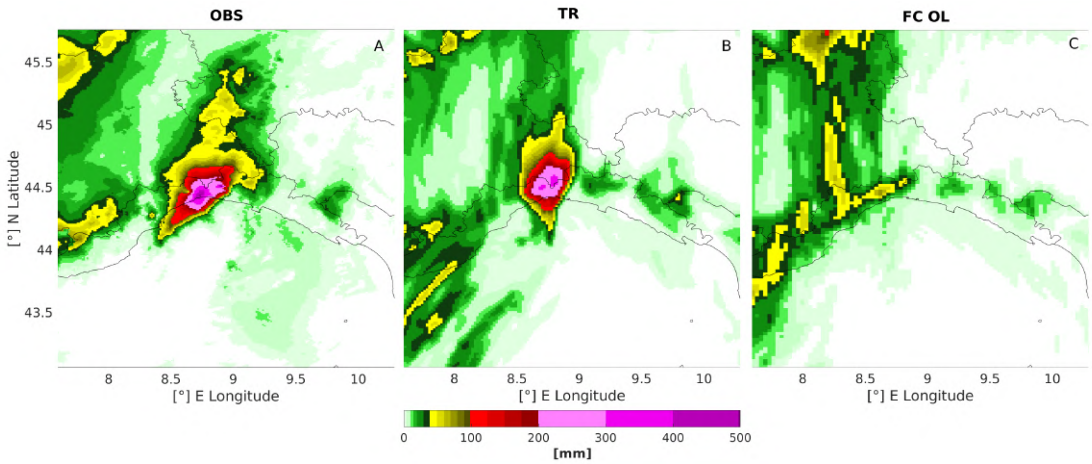

Figure 4. 12 hours accumulated rainfall between 21 UTC of the 14th of October and 09 UTC of the 15th from the merged radar and rain-gauges observation OBS (Panel A), the TR (Panel B) and from the FC_OL (Panel C).

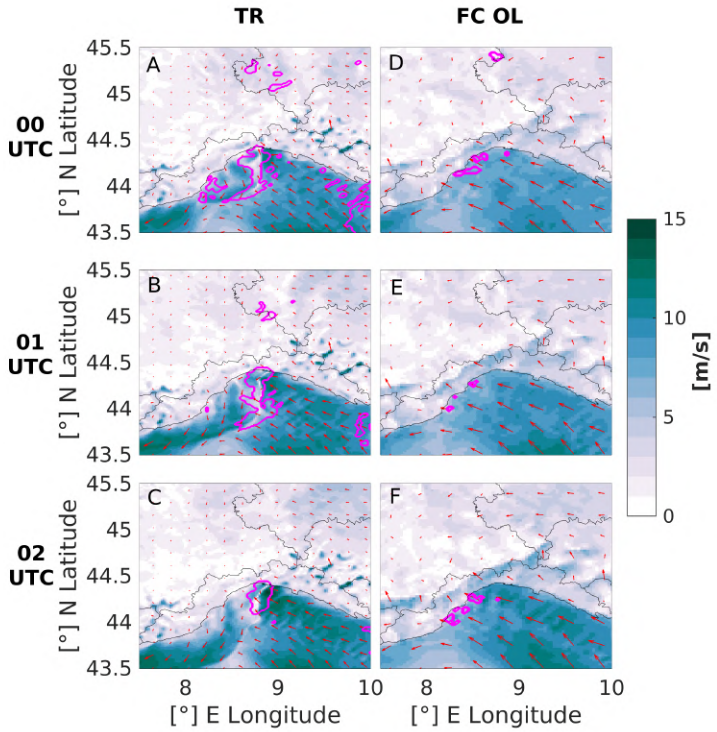

Figure 5. Wind field (colors and arrows) and ZTD 252 mm isoline (magenta line) from the TR (A, B, C) and from the FC_OL (D, E, F) in three hours of the main phase of the event: 00 UTC (A, D), 01 UTC (B, E) and 02 UTC (C, F) of the 15^{th} of October.

3.3. *Synthetic observations description and retrieval from the TR*

All the observations used in this work, namely the Hydroterra-like and the GNSS ZTD are synthetic observations retrieved from the TR fields. ZTD can be modeled as the difference between the distance in the zenith direction covered by an electromagnetic signal assuming to be in vacuum, i.e. moving with constant velocity c, and the actual distance, i.e. that covered at the actual velocity $v \leq c$. In particular, it can be expressed as the vertical integral of the atmospheric refractivity N [77], namely

$$\text{ZTD} = 10^{-6} \int N(z) dz, \tag{1}$$

where N is a function of the pressure of dry air p_d, the partial pressure of water vapour e, and the temperature T along the zenith profile :

$$N(z) = k_1 \frac{p_d(z)}{T(z)} + k_2 \frac{e(z)}{T(z)} + k_3 \frac{e(z)}{T(z)^2}. \tag{2}$$

The $k_i, i = 1, 2, 3$ constants are experimentally determined and, in this work, their values are taken from Smith and Weintraub [78] and Bevis *et al.* [79], in agreement with the WRF implementation. ZTD is related to IWV through

$$\text{ZTD} = \text{ZHD} + \text{ZWD} = \text{ZHD} + \text{IWV}/\Pi, \tag{3}$$

where ZHD is the Zenith Hydrostatic Delay, which is substantially controlled by the surface pressure [80], ZWD is the Zenith Wet Delay, which is controlled by the highly variable water vapor content, and Π is a conversion factor. It depends on the vertical mean value of the inverse of the temperature weighted by the water vapor density and is approximately equal to 0.15 [77,79]. To go from ZTD to IWV, thus, it is clear that additional information on surface pressure and temperature is needed. As these observations are sometimes hard to retrieve and they add processing steps that can be avoided by directly assimilating ZTD in the model, in all the experiments of this work, the assimilated variable is ZTD.

The Hydroterra-like ZTD is assimilated only over land, since Hydroterra will not retrieve ZTD over the sea. This is mainly because the ZTD InSAR maps (as the Hydroterra ones) are derived by taking phase differences for of each pixel using multi-temporal observations. The phase is the optical path delay and the own target's signature, which should be stable in the time between the two SAR observations, in order to provide a reliable measure of the differential path delay. This does not occur when observing water, where the kinematic instability of the surface changes its radar reflectivity within milliseconds [81,82]. In SAR interferometry, water surfaces have random phase, even when observed by a very short revisit.

To obtain the GNSS-like ZTD the TR ZTD field is interpolated on the positions of the receivers of the Italian GNSS network, with a nearest-neighbour approach. The inter-distance between the GNSS receivers of the Italian network is between 30 and 50 km, and for a map of the receivers the reader is referred to Figure 4 of Lagasio *et al.* [22].

As with many heavy rainfall events, this case study was completely missed by Sentinel-1: the first observation was at 5.35 UTC of the 14th of October, too early to give some information for such very localised event, and the second one was at 5.25 UTC of the 15th of October, when the event was already over. The difficulty to find a case study in which to assimilate Sentinel-1 ZTD map with a timely passage [22,66] is due to its very low temporal resolution with respect to the dynamics of this kind of explosive high impact weather events.

3.4. Data assimilation setup and experiments configuration

The data assimilation procedure is performed with the state-of-the-art 3DVAR WRFDA package, V3.9.1 [83]. The 3DVAR finds the optimal estimate of the atmospheric state, called 'analysis', by minimising an appropriate cost function that weights the background atmospheric state(coming from a NWP model run) and the observations, by their uncertainties. A technical description of the assimilation procedures used in this study is given in Appendix A.

It has been shown that when high resolution radar observations are assimilated, if the cost function is not properly constrained, such a large number of inputs can dominate the analysis result by adding large unbalanced wind increments, especially when convective systems are present [84,85]. Also the high resolution ZTD Hydroterra-like observations can lead to unrealistic dynamics, by changing the atmospheric stability and producing very vigorous vertical motion throughout the domain (not shown). This is why an additional constraint in the assimilation procedure is needed.

The additional constraint used is sensitive to the large-scale features. It is well known that one of the challenges in convective-scale data assimilation is to extract as much information as possible from the observations while maintaining the background large-scale balance. In other words, the problem is to find a way to add high resolution observational data to the initial conditions through a data assimilation system without damaging the large-scale pattern, nor causing spurious convection [84]. A possible solution to improve the data assimilation procedure is to use a method to minimise the imbalance problem in the 3DVAR system by adding a constraint in the cost function using information at larger scales. This is defined in terms of the departure of a high resolution 3DVAR analysis from a coarser-resolution large-scale analysis, as explained more in detail in Appendix A [84]. In this work, the version of large-scale constraint (LSC) used in Tang *et al.* [85] is adopted. Firstly, the GFS forecast fields (instead of analysis fields) are interpolated into the same regular grids as the outer domain via the WRF pre-processing system. Secondly, they are assimilated as bogus observations in the inner domain during the regular DA cycles. Note that, as discussed in Appendix A, not all the grid points of the large domain are considered. In particular, in the present work, the LSC sampling step is set to 45 km, corresponding to retaining every second point of the d01 grid.

The assimilation experiments are performed sampling the observation at different spatial (2.5 km, 5 km, GNSS network location) and temporal (3 h, 6 h) resolutions in all the possible combinations. Table 1 introduces the experiments and Figure 6 shows a schematic of the OSSEs data assimilation timing. Note that in the first 6 hours the OSSEs have no assimilation due to the TR spin-up. The lower spatial resolution is set to 2.5 km (the FC resolution) because higher resolution violates the assumption of spatially independent observation errors for the **R** matrix [19,21,22].

Table 1. Short description of the OSSEs to determine the optimal spatio-temporal resolution of the Hydroterra-like ZTD observations.

Experiment	Assimilated ZTD	Obs. resolution	DA cycling interval	LSC activated
FC_OL	run without data assimilation			
FC_DA_2.5km_3h	Hydroterra-like	2.5 km	3-hour	yes
FC_DA_5km_3h	Hydroterra-like	5 km	3-hour	yes
FC_DA_gnss_3h	GNSS	GNSS Italian network	3-hour	no
FC_DA_2.5km_6h	Hydroterra-like	2.5 km	6-hour	yes
FC_DA_5km_6h	Hydroterra-like	5 km	6-hour	yes
FC_DA_gnss_6h	GNSS	GNSS Italian network	6-hour	no

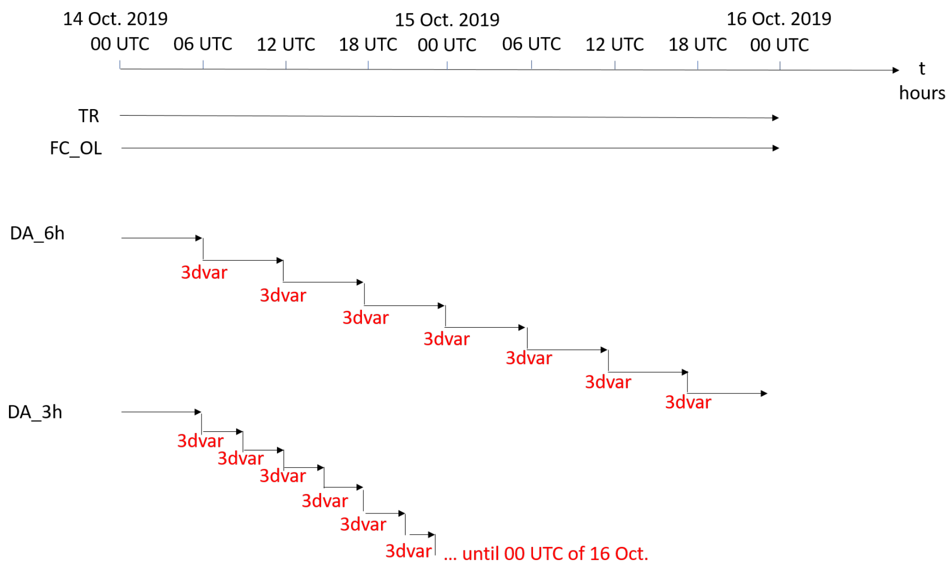

Figure 6. Schematic of the OSSEs assimilation timing. TR and FC_OL have no assimilation cycles, while DA_6h and DA_3h denote a generic assimilation experiment with assimilation every 6 and 3 hours, respectively.

3.5. Validation Method

The evaluation of the assimilation performances is done using the MODE tool [86,87], by comparing the TR accumulated rainfall field with the forecast fields of the other runs. The main advantage of such a validation is that the forecast is not only evaluated point-wise but also at feature level, thus overcoming the so-called "double-penalty" issue [88]. MODE identifies precipitation structures above given thresholds in both the forecast and the observed fields and performs a spatial evaluation of the model capability of reproducing the identified objects [22]. Especially for high resolution observations and cloud-resolving meteorological forecasts during deep convective events, it is preferable to use feature-based verification techniques, such as MODE, because traditional methods cannot provide a measure of spatial and temporal match between observed and forecast fields.

In this work, to evaluate the ZTD assimilation performances, 10 different indices are considered above 48 mm threshold. They include both pairs of object attributes and classical statistical scores, namely, for the geometrical indices we consider: centroid distance (CENTROID_DIST), angle difference (ANGLE_DIFF), area ratio (AREA_RATIO), symmetric difference (SYMMETRIC_DIFF), intersection area (INTERSECTION_AREA) and union area (UNION_AREA), while for the classical statistical indices we consider: Frequency BIAS (FBIAS), Probability of Detection Yes (PODY), False Alarm Ratio (FAR) and Critical Success Index (CSI). For a complete description of the indices refer to References [22,65,76].

4. Results

Looking at the 10 m wind field in the first hours of the event (Figure 7) it is possible to see that the presence or the absence of the convergence line over the sea is one of the most evident differences between the forecasts. As previously discussed, the convergence line is strong and persistent in the TR (Figure 7 Panels A, I, Q). It is interesting to underline that from a strictly forecasting view point, Poletti *et al.* [89] identify the presence of a convergence line over the sea as one of the most important factors that leads to the issue of a hydro-meteorological alert, as argued in what follows.

As discussed in Section 3.2, the convergence line is completely absent in the FC_OL simulation (Figure 7 Panels B, J, R). It is found that, the higher the spatio-temporal resolution of the assimilated ZTD field, the better the impact on the convergence line dynamics. In fact, assimilating the Hydroterra-like ZTD at 2.5 km grid spacing, in simulations FC_DA_2.5km_3h (Panels C, K, S) and FC_DA_2.5km_6h (Panels F, N, V), produces the most realistic convergence line. In particular, the convergence line is better defined by assimilating every 3 hours, although in both cases it is still different from the TR one. Assimilating the Hydroterra-like ZTD at 5 km grid spacing, as in the FC_DA_5km_3h (Panels D, L, T) and FC_DA_5km_6h (Panels F, N, V) runs, introduces smaller improvements in the modelling of the convergence line with respect to the previous experiments, while assimilating the ZTD at the GNSS locations in simulations FC_DA_gnss_3h (Panels E, M, U) and FC_DA_gnss_6h (Panels H, P, X) seems not to influence the surface wind dynamics at all. A better representation of the surface wind field in FC_DA_2.5km_3h (Panels C, K, S) and FC_DA_2.5km_6h (Panels F, N, V) is also accompanied by an increase of water vapor along the convergence line, more similar to the TR, as highlighted by the 252 mm isoline in Figure 7.

Lagasio *et al.* [22] showed that, for a similar back-building MCS that caused the severe Livorno 2017 flood, the ZTD assimilation from GNSS provided significant improvements in the heavy rainfall forecast. In particular, it was found that the GNSS ZTD assimilation was more effective when the wind field was simultaneously assimilated. This, together with the present findings, suggests that the coarse spatial resolution of the GNSS receivers helps in the correct modelling of the total amount of water vapor, which acts as a source for the heavy rainfall, but struggles in reproducing the fine-scale water vapor spatial distribution, that modifies the surface dynamics. This is especially true when, as in this case, the FC_OL dynamic is very far from the TR one. Thus, only by assimilating the Hydroterra-like ZTD observations at high spatial resolution, does the FC dynamic move towards the TR one showing a convincing intense convergence line.

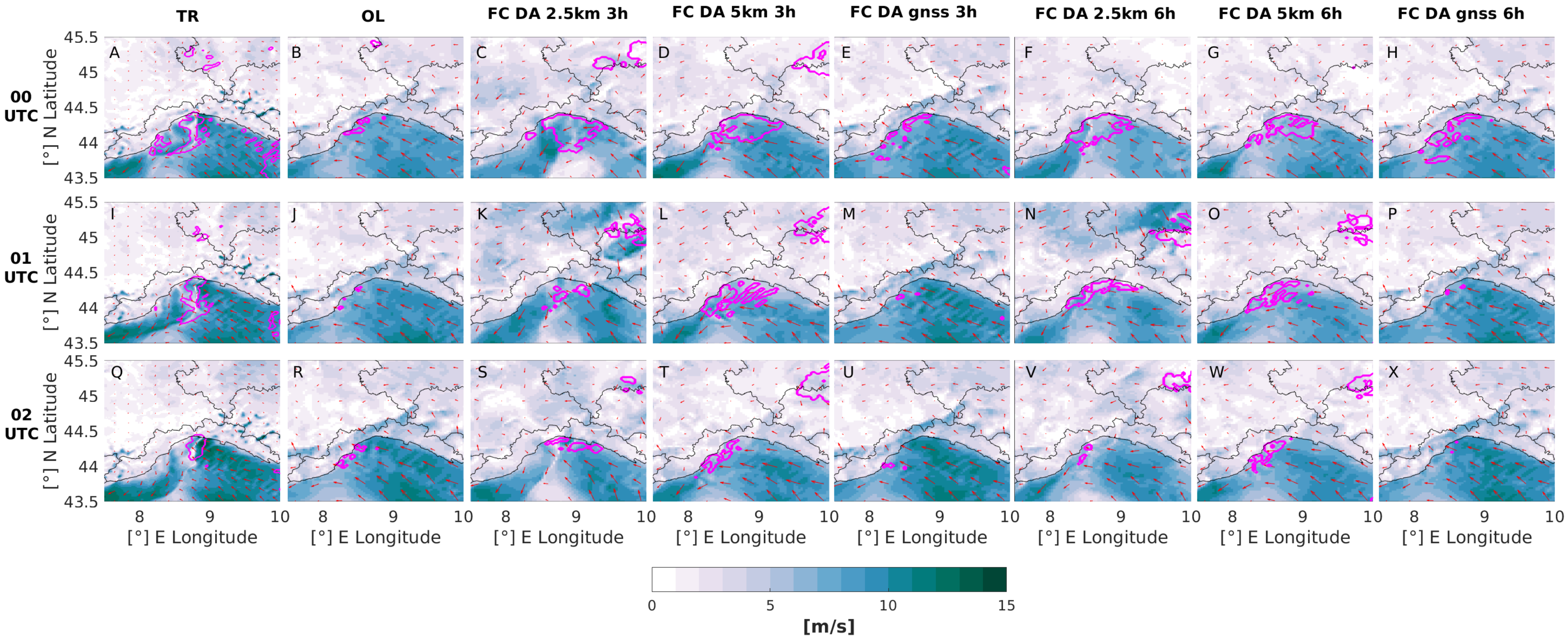

Figure 7. 10 m wind field (colors and arrows) and ZTD 252 mm isoline (magenta line) comparison during the main phase of the event: 00 UTC (first row), 01 UTC (second row), 02 UTC (third row) between TR (Panels A, I, Q), OL (Panels B, J, R), FC_DA_2.5km_3h (Panels C, K, S), FC_DA_5km_3h (Panels D, L, T), FC_DA_gnss_3h (Panels E, M, U), FC_DA_2.5km_6h (Panels F, N, V), FC_DA_5km_6h (Panels G, O, W), FC_DA_gnss_6h (Panels H, P, X).

Thus, the effects of the ZTD assimilation on the surface wind dynamics have direct impacts on the forecast of the rainfall pattern (Figure 8). In particular, the presence of the well-defined surface convergence line when assimilating the ZTD at 2.5 km grid spacing, in experiments FC_DA_2.5km_3h and FC_DA_2.5km_6h, results in a more localized rainfall pattern (Panels B and F, respectively). Although being weaker, this is very consistent with the TR rainfall field, which shows the typical V-shape pattern of the Ligurian MCSs [4]. Assimilating a coarser ZTD product, namely the Hydroterra-like ZTD at 5 km, in the FC_DA_5km_3h (Panel C) and FC_DA_5km_6h (Panel G) runs, results in a rainfall pattern that is more localised than the OL one, but less than in the above mentioned 2.5 km experiments. With respect to the FC_DA_2.5km experiments, the rainfall peak appears to be shifted westward. Concerning the simulation of the surface convergence field, the assimilation of ZTD at the GNSS locations, in the experiments FC_DA_gnss_3h (Panel D) and FC_DA_gnss_6h (Panel H), instead, maintains a more widespread rainfall pattern very similar to the FC_OL one. Note that the time intervals of the rainfall accumulation are different. In the TR the 12 hour accumulation interval is between 21 UTC of the 14^{th} and 09 UTC of 15^{th} of October. In the FC experiments, instead, it is between 00 and 12 UTC of the 15^{th} of October. The reason for this is because in the FC runs, despite the assimilation procedure, a temporal shift of roughly three hours of the intense rainfall remained.

None of the FC simulations is able to reach the TR accumulated rainfall peak values. However, the assimilation of Hydroterra-like observations at 2.5 km (FC_DA_2.5km_3h and FC_DA_2.5km_6h) allows a big improvement with respect to the OL run as quantitatively highlighted by the Method for Object-Based Evaluation (MODE) rainfall validation.

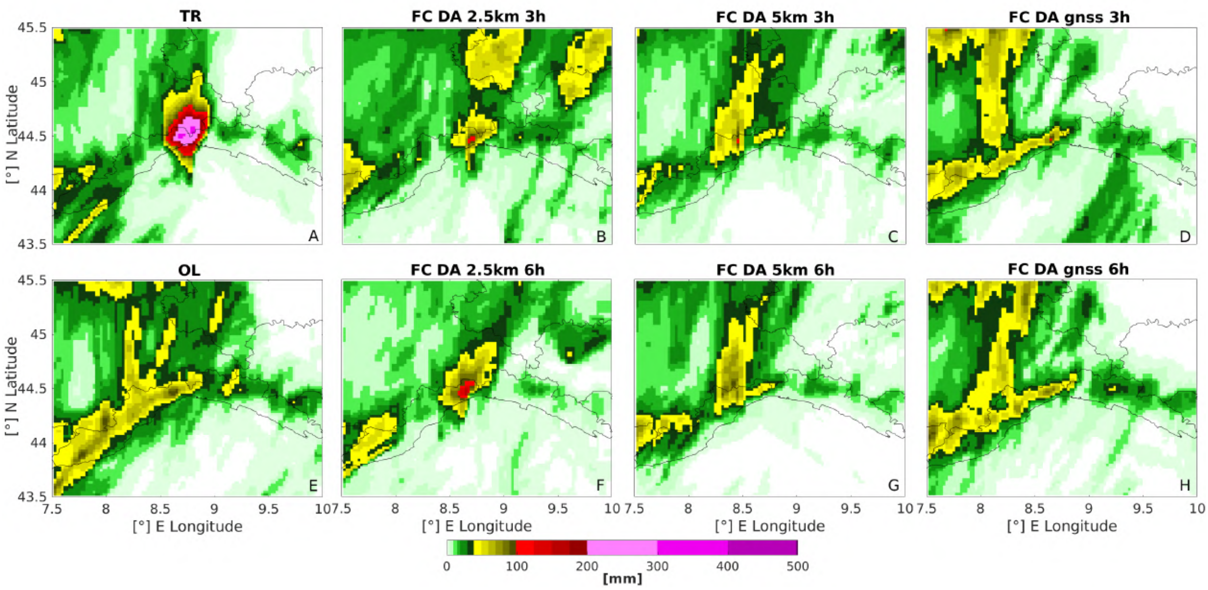

Figure 8. 12-hours accumulated rainfall comparison. A: TR, B: FC_DA_2.5km_3h, C: FC_DA_5km_3h, D: FC_DA_gnss_3h, E: OL, F: FC_DA_2.5km_6h, G: FC_DA_5km_6h, H: FC_DA_gnss_6h. In the TR (Panel A) the time window is between 21 UTC 14 Oct and 09 UTC 15 Oct, while in all the other cases is between 00 and 12 UTC 15 Oct.

Figure 9 shows statistical indices that evaluate all the objects in the whole domain of Figure 8. It is possible to see that the 48 mm threshold (Figure 9) reveals that when assimilating the Hydroterra-like ZTD observation at 2.5 km, the accumulated rainfall structure is better captured by the model (higher POD, CSI and better FBIAS and FAR), with respect to assimilating the same observation at 5 km grid spacing. In particular, assimilating at 2.5 km every 6 hours provides the lowest FAR, due to a correct spatial distribution of the rainfall field. In fact, with respect to the simulation assimilating at 2.5 km every 3 hours, no rainfall overestimation is produced inland (north of 45°N, as visible in Panels B and F of Figure 8). This is probably due to the eastward displacement of the convergence line at 1UTC (Figure 7K), that is strongly reduced in the FC_DA_2.5km_6h (Figure 8F) forecast. In fact, the FC_DA_2.5km_6h has a weaker convergence line (Figure 7 Panels C, K, S) with respect to the FC_DA_2.5km_3h (Figure 7 Panels F, N, V), that is, however, more persistent in terms of location.

The validation in terms of the MODE geometrical indices is restricted to the core rainfall object, and not to the entire WRF innermost domain, d03. This procedure cannot be completely automated because it is specific for each event. It is also necessary to focus the validation on the area of interest, instead of the full WRF grid, in order to avoid mixing the multiple rainfall objects that appear in the simulation results, which could affect the validation results. Looking at these geometrical indices (Figure 10) it is possible to see that the angle difference (ANGLE_DIFF) of the FC_OL and the FC_DA_gnss runs are the worst ones, remarking a more widespread rainfall pattern with respect to the TR one. The CENTROID_DIST and the SYMMETRIC_DIFF highlight how the simulations assimilating Hydroterra-like observations at 2.5 km resolution (FC_DA_2.5km_3h and FC_DA_2.5km_6h) produce a better localised intense rainfall object, with a shape closer to the TR one. Furthermore, the INTERSECTION_AREA shows that the FC_DA_2.5km_6h has a better pattern extent.

Summarizing, it is possible to say that assimilating the ZTD Hydroterra-like observations produces the best improvement in a very challenging forecast, where the dynamical and thermodynamical differences between FC_OL and TR are large. In particular, the higher spatial resolution (2.5 km) seems to be the most effective in changing the wind dynamics and, consequently, the rainfall pattern. Both temporal resolutions of the assimilation (3 and 6 hours) produce this improvement. However, the simulation assimilating every 3 hours (FC_DA_2.5km_3h) still maintains a high FAR due to the shifting of the simulated convergence line. Instead, a more persistent convergence line in the simulation with data assimilation performed every 6h (FC_DA_2.5km_6h) gives a lower FAR (Figure 9).

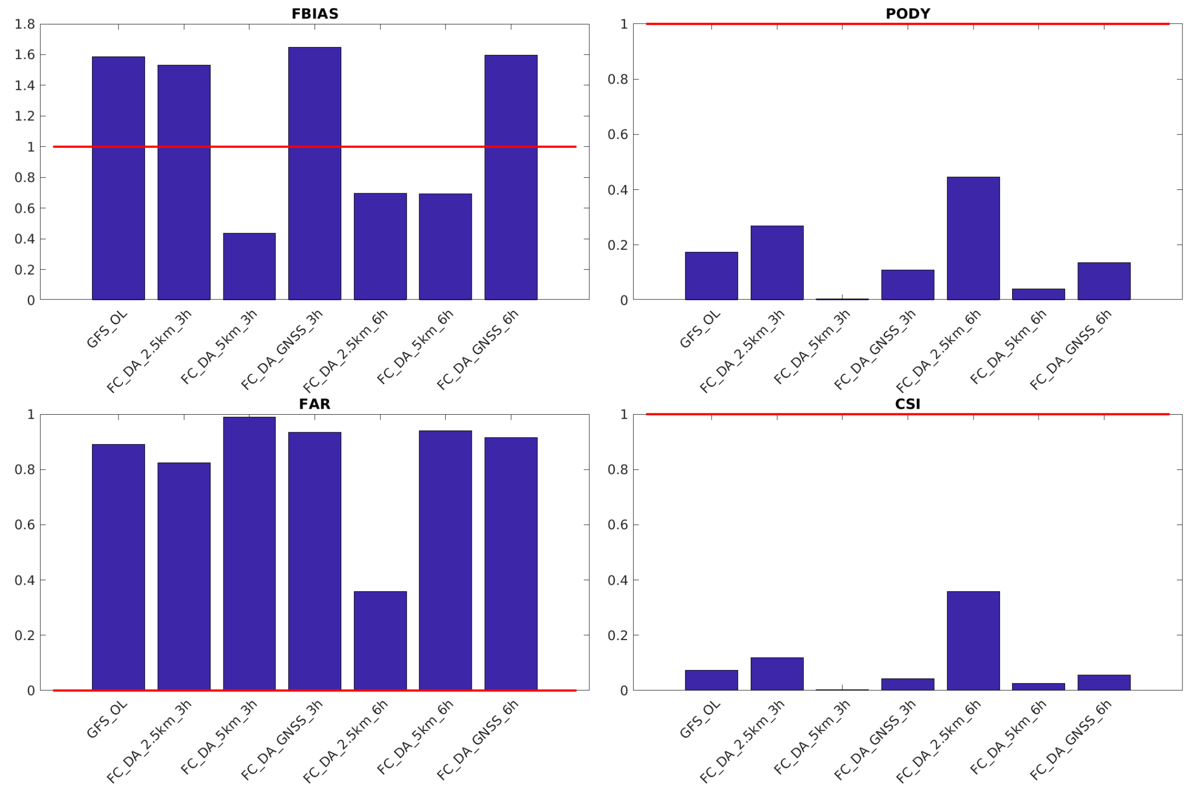

Figure 9. OSSEs statistical MODE indices for the 48 mm threshold. The red horizontal lines indicate the ideal scores.

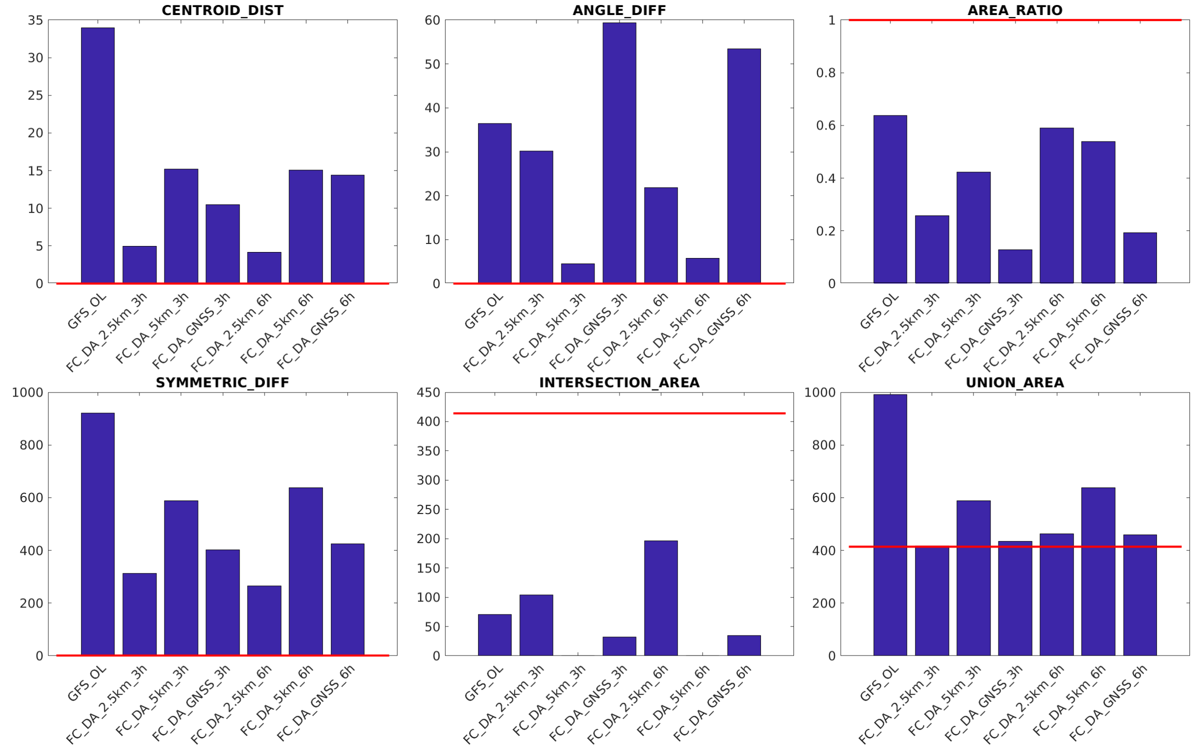

Figure 10. OSSEs geometrical MODE indices for the 48 mm threshold. The red horizontal lines indicate the ideal scores.

5. Discussion

Only the high resolution Hydroterra-like observation experiments are capable of changing the OL dynamics enough to provide some of the main ingredients that are important to forecast this kind of back-building MCS. As previously outlined, the MODE analysis indicate that the 6-hour assimilation experiment has better performance than the 3-hour one. This suggests that a 3-hourly DA cycle may not leave enough time for a proper dynamical adjustment to the new humidity information, which can be reached with a 6-hourly cycle. Thus, it appears that the assimilation of the Hydroterra-like ZTD modifies the dynamics at the mesoscale, so that the environment is properly set for the development of the convective V-shape storm.

Due to the characteristic low predictability of this kind of event, Liguria region's meteorological forecaster developed a check-list tool [89] to consider various ingredients indicating the possible occurrence of severe, organized, and stationary storms, like the back-building MCSs, during the operational forecasting activities.

To assess the impact of assimilating Hydroterra-like observations, the TR, OL and FC_DA_2.5km_6h runs are compared following Table 2 of the checklist by Poletti *et al.* [89]. In the first part (a) of this table, an analysis of some thermodynamic parameters such as the K-Index (KI), the Total totals (TT), the CAPE and the Precipitable Water (PW) allows to evaluate the probability of severe thunderstorms (see Poletti *et al.* [89] for their definitions). If some of these parameters exceed the identified thresholds, the second part of the table (b) is used to evaluate whether the event under consideration is likely to be organized and persistent. Some of the parameters that are considered in this second part are the presence of a wind convergence line over the sea for more than 3 hours, and the strength of the 950 hPa temperature (and humidity) gradient between the Po Valley and the Ligurian Sea. In this work, the use of both parts of Table 2 of Poletti *et al.* [89] (the checklist) allows to evaluate the impacts that assimilating the high resolution Hydroterra-like ZTD maps has on some physical quantities that are relevant for operational applications.

It is worth noticing that even if specific thresholds are identified in the Poletti *et al.* [89] checklist, their values need to be interpreted. For example, the CAPE parameter threshold should be modulated on the annual cycle, as summer events are usually characterised by higher CAPE values than autumn ones. Furthermore, the K-index is mentioned as a good indicator of severe and organized thunderstorms, but not for persisting ones, like this kind of back-building MCSs. Also the TT index and the CAPE do not show a relevant predictive ability for persistent events because for almost the whole data sets their values fall within the respective low ranges. Thus, these indices are here used to evaluate if the simulations produce scenarios leading to severe events with respect to some metrics that are currently used for operational activities. The presence of the persistent convergence line and the surface humidity gradients are evaluated to analyse if the event can be both organized and stationary (meaning that it is more prone to generate flash floods).

A representative point within the moist and conditionally unstable air mass in the Ligurian sea is chosen to produce the Skew-T diagram and to calculate the relevant indices of the Poletti *et al.* [89] checklist. The virtual vertical soundings are shown in Panels A-C of Figure 11, while the corresponding surface water vapor mixing ratio maps are shown in Panels D-F. The soundings are taken in the early phase of the event, which are a few hours apart depending on the configuration, as discussed above. In particular, the virtual sounding is taken at 4 UTC in the TR experiment and at 7 UTC of the 15th of October in the FC_OL and FC_DA_2.5km_6h experiments.

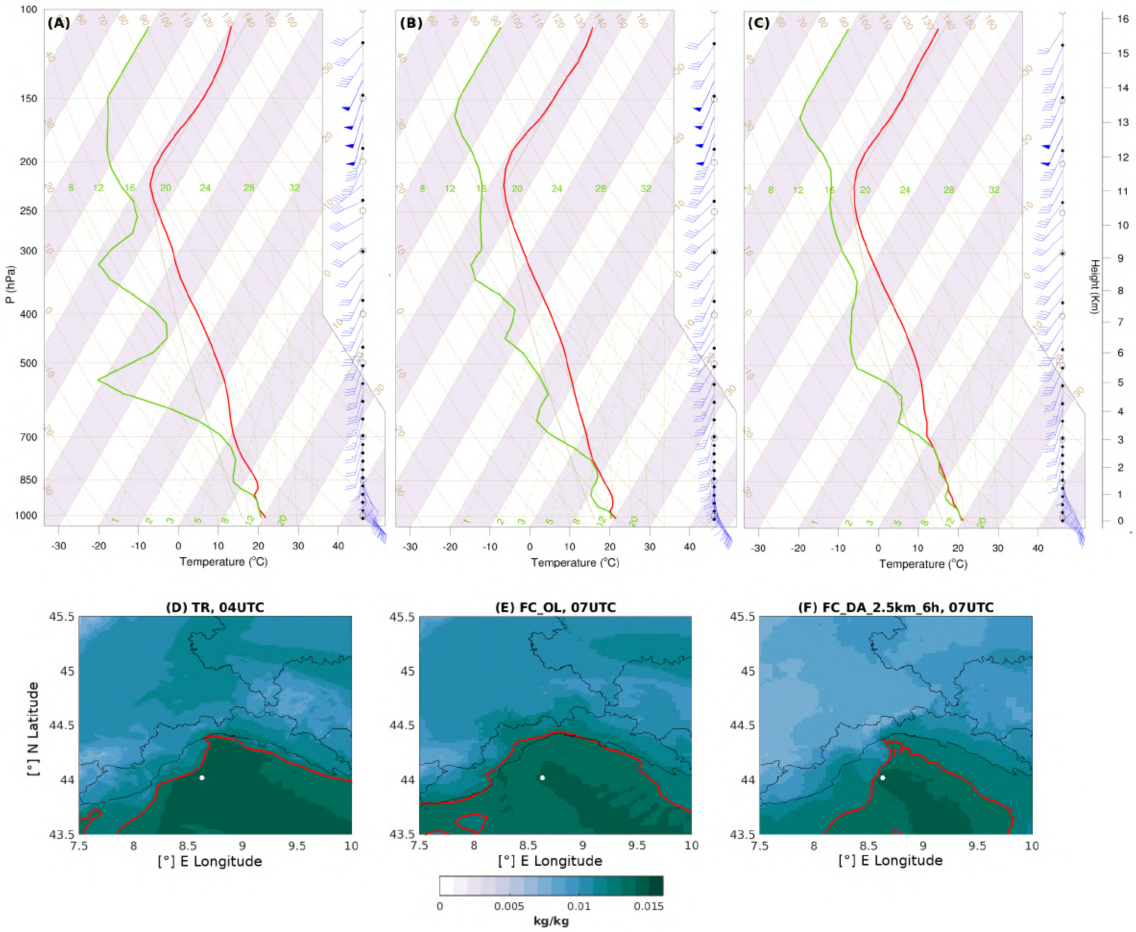

Figure 11. First row: Skew-T diagrams for TR (A), FC_OL (B) and FC_DA_2.5km_6h (C). Second row: Q2m instantaneous field with the 0.013 kg/kg isoline in red for TR (D), FC_OL (E) and FC_DA_2.5km_6h (F). The white dots indicate the point where the Skew-T are calculated. The TR is investigated at 04:00 UTC while the FC_OL and the FC_DA_2.5km_6h are taken at 07:00 UTC.

While the TR and the FC_DA_2.5km_6h runs are characterised by thermodynamic indices that fall in the moderate to high ranges, the FC_OL has generally weaker values. For example, the CAPE over the Ligurian Sea in the TR and FC_DA_2.5km_6h runs is of the order of 2000 J kg^{-1} and it is only around 1500 J kg^{-1} in the FC_OL. The KI is moderate for the TR and FC_DA_2.5km_6h runs, with values around 30°C, and is weak for the FC_OL, roughly 25°C. The TT and the PW indices, instead, do not highlight significant differences, as they all fall in the same range (weak for the TT, between 45 and 50°C, and moderate for the PW, between 30 and 35 mm). Thus, the first part of the checklist evaluation suggests that severe events can occur in all forecasts, with the FC_OL generally having weaker indices.

Moving to the organization and persistence evaluation, Poletti *et al.* [89] highlights the importance of the presence of the convergence line for more than three hours over the sea. In fact, this persistent dynamics is responsible for the development of convective cells over the same location, producing very high values of accumulated rainfall. The fact that in the TR the convergence line lasts for at least three hours is visible in Panels A, I, Q of Figure 7, showing the surface wind field between 0 and 2 UTC, and in Panel D of Figure 11, showing the surface water vapor mixing ratio field (at 2 m, Q2m) at 4 UTC. In particular, the surface convergence is highlighted by the 0.013 kg/kg isoline shown in red, which marks the dividing line between the drier continental air mass and the moist maritime one. The FC_OL simulation does not present any sign of convergence line, neither at the beginning of the event (Figure

7, Panels B, J, R), nor during its main phase, as indicated by the more homogeneous Q2m distribution over the sea at 7 UTC (Figure 11E), with the 0.013 kg/kg isoline closely following the coastlines. The FC_DA_2.5km_6h simulation shows the presence of the convergence line (Figure 7 Panels F, N, V) since the beginning of the event. Even if weaker and slightly shifted with respect to the TR, the convergence line is clearly visible for at least three hours, and it strengthens at 7 UTC, as revealed from the Q2m distribution shown in Figure 11F.

Thus, this important ingredient, associated with the presence of a temperature gradient (not shown) and a Q2m gradient between the Po Valley and the Ligurian Sea (Figure 11D-F) allows us to conclude that the TR and the FC_DA_2.5km_6h simulate a severe organized and persistent event (consistent with the back-building MCS dynamics) while the FC_OL simulates a weaker and non-organized event. This analysis, using physical criteria that are relevant for operational activities, shows that the assimilation of Hydroterra-like observations is able to change the model dynamics and thermodynamics so that, starting from a run that simulates a relatively weak, widespread, and non-organized rainfall event, a realistic back-building MCS is produced.

Note that the FC_DA experiments are not fully operational configurations, as the Hydroterra-like ZTD is assimilated during the event. Future works will be devoted to study the impact of assimilating the Hydroterra-like ZTD product in fully operational configurations, taking into account, for example, the availability of the forecasts and of the Hydroterra products. In this way, a more precise quantification of the lead time of the improved forecast in different meteorological conditions could be performed.

The proven relevance of the Hydroterra-like observations, albeit structurally retrievable only over the land, can be further interpreted in light of the results of Chu and Lin [90], and Chen and Lin [91]. These authors identified four moist flow regimes for a (two-dimensional) conditionally unstable flow over a mesoscale mountain ridge and proposed an unsaturated moist Froude number $F_w = U/(hN_w)$ as the control parameter for these flow regimes, where U is the wind speed, h the mountain height and N_w the moist Brunt-Väisälä frequency. In the regime with low F_w, the quasi-continuous and heavy rainfall is produced over the upslope side of the terrain as individual convective cells develop upstream at the head of the density current, thus resembling the typical back-building MCS scenario over the Mediterranean area. Propagating precipitation is caused by convection triggered ahead of the hydraulic jump over the lee slope, in this case coincident with the seaward side of coastal mountain range, and is advected by the basic large-scale flow. Thus, the aforementioned hydraulic jump is controlled by downstream conditions over the land, then supporting of the relevance of continental Hydroterra-like observations. This means that the assimilation of ZTD observations over land modifies the thermodynamical state of the upstream flow, which significantly impacts the surface wind dynamics over the Ligurian Sea, as shown in Figure 7 and discussed previously. To explicitly show the link between the mesoscale dynamics and the convective dynamics in this region characterized by complex terrain, Figure 12 shows the surface wind speed and the isosurfaces of the updraft (green) and downdraft (gold) velocities at 1 m/s in the TR, FC_OL and FC_DA_2.5km_6h experiments. As visible in the figure, the FC_OL run is the only one that does not produce ascending motion with a narrow and well organized structure along the surface wind convergence line.

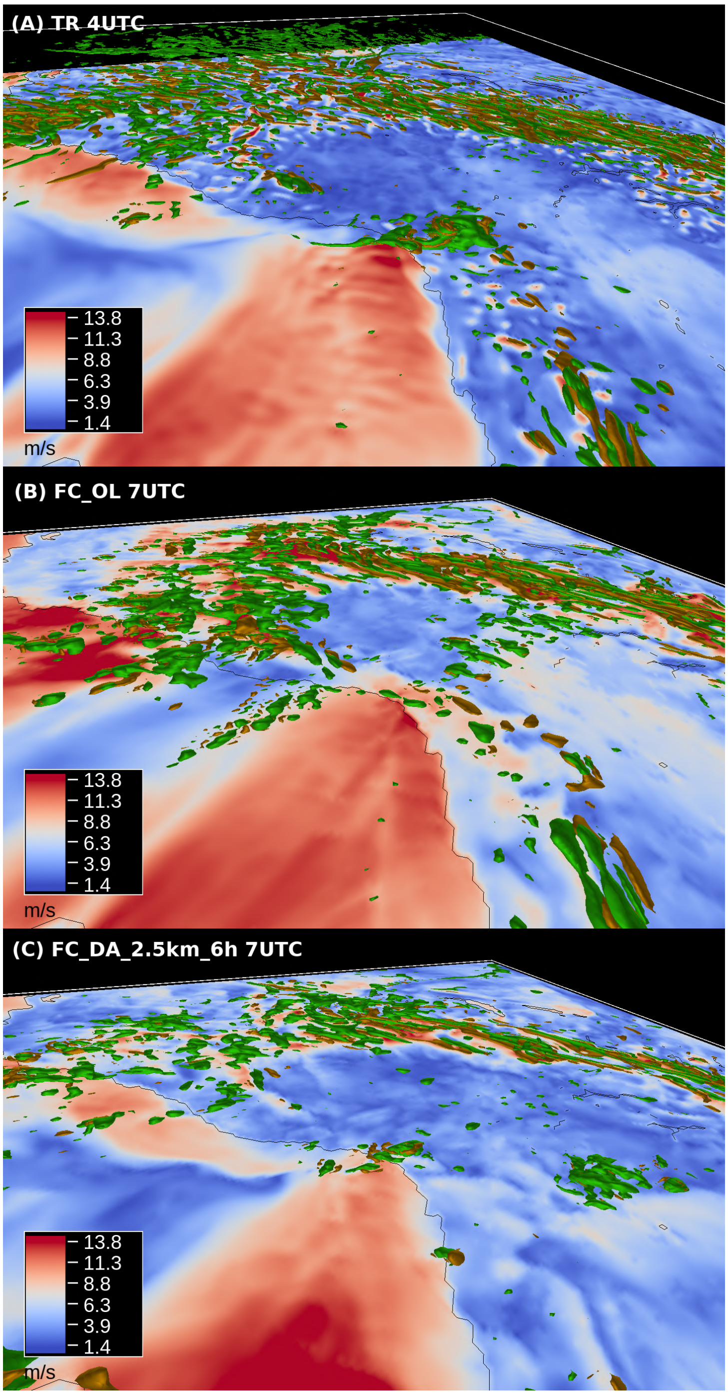

Figure 12. Rendering of the surface wind speed (colors) and vertical updrafts (green isosurfaces at 1 m/s) and downdrafts (gold isosurfaces at -1 m/s) for TR at 4 UTC (A), FC_OL (B) and FC_DA_2.5km_6h (C) at 7 UTC on the 15th of October 2018.

6. Conclusions

The main goal of the present work is to evaluate the possible added value of directly assimilating in a NWP model the high resolution ZTD estimates that will be provided by the SAR sensor flying on board of the Hydroterra geosynchronous satellite, an ESA 10th Earth Explorer mission candidate. Firstly, a set of OSSEs is built to identify the spatio-temporal resolution of the new ZTD observations that has the largest positive impact on the forecast of a heavy rainfall event. Secondly, a comparison with the improvements induced by the assimilation of ZTD from the currently available GNSS Italian network is performed for the same case study. All validations are done both in a qualitative way by looking at appropriate maps, and in a quantitative way using an object-based diagnostic tool applied to the accumulated rainfall field [86,87, MODE].

The case study is a MCS that occurred over the Liguria region between the 14th and the 15th of October 2019, characterized by a very low predictability. As in the present case, MCSs are often triggered by the encounter of a cold and dry continental air mass and an unstable, moist and warmer maritime air mass [4], resulting in a persistent and well-defined surface wind convergence line. The reference TR is performed using an initialization and a setup allowing to obtain a good representation of the real extreme event, with very intense accumulated rainfall values over a relatively small area. Conversely, the FC_OL is not able at all to model this event and its dynamics differ significantly from the TR, with the convergence line completely missing in the FC_OL.

The OSSEs highlight that, even if the starting point (the FC_OL) completely lacks some of the fundamental ingredients for a skilful forecast of a back-building MCS, the assimilation of high resolution (at 2.5 km) Hydroterra-like observations is able to deeply improve the forecast. In fact, this is the only observation, among the ones used in this work, that modifies the wind dynamics so that a persistent and well-defined convergence line is modelled. This is particularly relevant because, although the Hydroterra-like ZTD observation is assimilated only over land, it is able to produce more realistic dynamics over the sea, which is crucial for a correct forecast of the MCSs. A better surface wind representation is accompanied by a more localized and more intense accumulated rainfall simulation that resembles the reference run more closely.

The comparison with the skills of the simulation assimilating the currently available GNSS receivers' ZTD observations (with a spacing of roughly 30-50 km) shows that it is indeed the fine spatial resolution that adds information to the model so that the surface wind and the accumulated precipitation are simulated more accurately.

It is worth noticing that none of the simulations reach the TR rainfall peak. However, it is well known that this kind of event is characterized by an intrinsic low predictability [3,4,43]. For this reason, in an operational framework, some regions particularly prone to this kind of event developed tools (in the form of a checklist) to account for all the relevant dynamical and thermodynamical processes that could help to forecast this kind of extreme event [89]. From the evaluation of the most important parameters highlighted in the Liguria region checklist, it appears that FC_OL and FC_DA_2.5km_6h are both indicating the likely occurrence of a severe event (with the FC_OL having a weaker signal), but only the FC_DA_2.5km_6h is able to suggest the probable occurrence of a severe, organized, and persistent event, as in the TR. In fact, one of the most important dynamical ingredients is the presence of a convergence line over the sea for more than three hours, and only by assimilating the Hydroterra-like observations at 2.5 km is the model able to reproduce it.

Summarizing, the Hydroterra-like observations are found to have great potential for use in a meteorological framework. In particular, the assimilation of such high spatio-temporal resolution information of water vapor (in form of ZTD) seems to be able to correct the model dynamics so that the heavy rainfall event is better reproduced. Such an influence in the model simulation can be important not only in the operational framework but also lead to deeper physical insights on the evolution of such events. In this work, the time resolution used for Hydroterra-like observations is 3 and 6 hours because a conservative approach in the the state-of-the-art assimilation procedure was selected. However, having hourly ZTD observations from Hydroterra could pave the way for various new applications such as: the implementation of ensemble NWP nowcasting chains with hourly initialization, the use of different kinds of data assimilation techniques to exploit the ZTD temporal evolution (i.e. 4DVAR), and the development of storm detection and prediction algorithms based on the spatial distribution of the water vapor field [92–94]. Furthermore, in this case, the impact evaluation is performed on an explosive rainfall event, but it is demonstrated that assimilating ZTD at high resolution is useful also to improve forecasts of slowly evolving rainfall cases [22].

Another important future development of this work would be to evaluate the added value of assimilating Hydroterra-like ZTD in other regions covered by the Hydroterra geostationary observations, e.g. Africa. West Africa, including the Sahel, is a good example because MCSs are frequent and can cause significant damage. Due to the lack of observations in that area, the Hydroterra ZTD observations could be very valuable for improving the forecast capabilities, especially when coupled with the Hydroterra soil moisture observations, because soil moisture plays a fundamental role in the dynamics of MCSs in this region [95]. In fact, the MCSs which form over land (e.g. in the Sahel where they are responsible for the majority of annual rainfall [96]) are known to be controlled by the surface properties [97]. The added value of the Hydroterra soil moisture observation in the hydrological framework have been discussed in [31]. Future works are needed to assess the impact of these new observations (ZTD and soil moisture) in a complete hydro-meteorological framework that is very important to forecast high impact weather events over areas with complex terrain, such as the Mediterranean region. Furthermore, also the differences and the interactions of these new data with other traditional sensors (e.g. radar and ground stations) will be investigated in future works.

Author Contributions: Conceptualization, A.P., A.M.-G., S.H., R.H.; methodology, M.L., A.N.M., A.P., G.B.; validation, A.N.M., G.B., L.P.; formal analysis, M.L.; investigation, M.L., A.N.M., L.P., A.P.; resources, A.P., G.B.; data curation, M.L.; writing-original draft preparation, M.L., A.N.M., A.P.; writing–review and editing, M.L., A.N.M., A.P., L.P., G.B.; visualization, M.L., A.N.M., G.B.; supervision, A.P., A.M.-G.; project administration, A.P., S.H., R.H.; funding acquisition, A.P., S.H., R.H.

Funding: This research was funded with the Hydroterra (former G-Class) phase-0 Science and Requirement project by ESA grant number 4000127280/19/NL/CT.

Acknowledgments: Thanks are due to LRZ Supercomputing Centre, Garching, Germany, where the numerical simulations were performed on the SuperMUC Petascale System, Project-ID: pr62ve. Two anonymous reviewers are acknowledged for their insightful comments. A. N. M. acknowledges support from the TWIGA project, which has received funding from the European Union's Horizon 2020 Research and Innovation Program under grant agreement No.776691.

Conflicts of Interest: The authors declare no conflict of interest.

Appendix A. Data assimilation procedures

The standard data assimilation 3DVAR technique implemented in the WRFDA package [83] looks for the minimum of the following cost function [98]

$$J(x) = \mathbf{J}_b + \mathbf{J}_0 = \frac{1}{2}\left(\mathbf{x}-\mathbf{x}^b\right)^T \mathbf{B}^{-1}\left(\mathbf{x}-\mathbf{x}^b\right) + \frac{1}{2}\left(\mathbf{y}-\mathbf{y}^0\right)^T \mathbf{R}^{-1}\left(\mathbf{y}-\mathbf{y}^0\right), \quad \text{(A1)}$$

in which $\mathbf{x}$ is the analysis, $\mathbf{x}^b$ is the first guess coming from a NWP model, $\mathbf{y}^0$ is the observation vector to be assimilated and $\mathbf{y} = \mathcal{H}(\mathbf{x})$ is the model-derived observation vector. $\mathbf{y}$ is obtained by applying the observation operator $\mathcal{H}$ on the analysis $\mathbf{x}$, namely $\mathbf{y} = \mathcal{H}(\mathbf{x})$. The solution of equation (A1) represents an *a posteriori* minimum variance estimate of the true state of the atmosphere given two sources of data: the numerical first guess $\mathbf{x}^b$ and the available observation $\mathbf{y}^0$. Their relative importance is weighted by the estimates of their errors contained in the background error covariance matrix, $\mathbf{B}$, and the observation error covariance matrix, $\mathbf{R}$. The $\mathbf{R}$ matrix is actually the sum of two distinct error covariance matrices: the observation (instrumental) matrix and the representativity error matrix (that contains the approximations introduced by geometrical transformations, interpolations, etc.). This matrix is assumed to be diagonal, as done in most of the models [99], implying that the correlations between different instruments and between different observations made by the same instruments are equal to zero.

In this work, the Control Variable option 7 (CV7) of the WRFDA package is used for the $\mathbf{B}$ matrix calculation with the National Meteorological Center (NMC) method [100]. In previous works, where ZTD from Sentinel and GNSS was assimilated [22,66], the CV5 option was used, instead. The CV5 option exploits the velocity potential and the streamfunction (ψ, χ) as momentum control variables. This has been shown to improve the representation of the large-scale features, thanks to the balance between the mass and wind fields, but the small-scale features are missed [101]. Instead, the CV7 option uses the wind components (U, V) as momentum control variables. In CV7, since no balance constraints are applied, the use of (U, V) as control variables can provide closer fitting to dense observations in limited area convective scale data assimilation experiments [101]. The NMC method is applied over the entire month of October 2018 with a 24-hour lead time for the forecasts starting at 00:00 UTC and a 12-hour lead time for the ones initialised at 12:00 UTC of the same day. The differences between the two forecasts ($t + 24$ and $t + 12$) valid for the same reference time are used to calculate the domains specific error statistics.

Concerning the Large-Scale Constraint (LSC), it is mathematically implemented into WRFDA 3DVAR by adding a new term $\mathbf{J}_c$ to equation (A1), namely, using the incremental formulation,

$$J(x) = \mathbf{J}_b + \mathbf{J}_0 + \mathbf{J}_c = \mathbf{J}_b + \mathbf{J}_0 + \frac{1}{2}\left(\mathbf{d}_c - \mathbf{HUv}\right)^T \mathbf{R}_c^{-1}\left(\mathbf{d}_c - \mathbf{HUv}\right), \quad \text{(A2)}$$

where $\mathbf{d}_c = \mathbf{y}_c - \mathcal{H}(\mathbf{x}_b)$ is the innovation vector that measures the departure of the LSC $\mathbf{y}_c$ from its counterpart computed from the background $\mathbf{x}_b$; $\mathbf{v} = \mathbf{U}^{-1}(\mathbf{x} - \mathbf{x}_b)$ is the control variable vector, with $\mathbf{U}$ being the decomposition of the background error covariance $\mathbf{B}$ via $\mathbf{B}$=$\mathbf{UU}^T$; and $\mathbf{H}$ is the linearization of the nonlinear observation operator $\mathcal{H}$. The $\mathbf{y}_c$ variable includes the meridional and zonal wind components, the temperature, and the water vapour mixing ratio from the large-scale analysis that are being assimilated as bogus observations. The errors for wind, temperature, and water vapour mixing ratio are 2.5 m s^{-1}, 2°C, and 3 g kg^{-1}, respectively, and are determined by the diagnostics of the GFS product [84,85]. They form the $\mathbf{R}_c$ matrix, which weights the importance of the LSC term in the cost function minimization.

Starting from the results obtained by Tang *et al.* [85], some experiments are performed as sensitivity, to understand the effect of the LSC scheme to different scales of the analysis fields and the precipitation forecast (not shown). In [85] the sensitivity on the assimilation scheme is performed using LSC every 1, 5, 10 grid points of the outer WRF domain (d01) at 15 km resolution and starting from different vertical levels. By skipping the first few levels in the LSC scheme, they allow the lower atmosphere to develop the small-scale dynamics that can be important for the convection development, due to, for example, the horizontal gradients of the surface fluxes and the interactions with the orography. Their best results are achieved sampling every 5 grid points (at, thus, 75 km grid spacing) and starting from the fourth vertical level. However, in all the experiments performed, the forecast is found to improve with respect to the open loop reference run.

In this work, the WRF d01 domain at 22.5 km resolution is used for LSC sensitivity retaining a value every 1, 2, and 3 grid points. Further experiments are performed by skipping the first few vertical model levels, to minimise the possible impact of the large scale constraint on the small-scale features and result in a more effective assimilation of surface observations. In this particular case, reproducing the same sensitivity of [85], no significant differences are highlighted skipping the lower three vertical levels (not shown). The final setup chosen for this work is the LSC sampling every 2 grid points of d01 without skipping any vertical level.

References

1. Gaume, E.; Borga, M.; Llassat, M.C.; Maouche, S.; Lang, M.; Diakakis, M. Mediterranean extreme floods and flash floods. https://hal.archives-ouvertes.fr/hal-01465740v2/document, 2016.
2. Rebora, N.; Molini, L.; Casella, E.; Comellas, A.; Fiori, E.; Pignone, F.; Siccardi, F.; Silvestro, F.; Tanelli, S.; Parodi, A. Extreme rainfall in the Mediterranean: What can we learn from observations? *J. Hydromet.* **2013**, *14*, 906–922.
3. Ducrocq, V.; Braud, I.; Davolio, S.; Ferretti, R.; Flamant, C.; Jansa, A.; Kalthoff, N.; Richard, E.; Taupier-Letage, I.; Ayral, P.A.; others. HyMeX-SOP1: The field campaign dedicated to heavy precipitation and flash flooding in the northwestern Mediterranean. *Bull. Amer. Meteor. Soc.* **2014**, *95*, 1083–1100.

4. Fiori, E.; Ferraris, L.; Molini, L.; Siccardi, F.; Kranzlmueller, D.; Parodi, A. Triggering and evolution of a deep convective system in the Mediterranean sea: Modelling and observations at a very fine scale. *Q. J. R. Meteor. Soc.* **2017**, *143*, 927–941. doi:10.1002/qj.2977.
5. Houze, R.A. 100 years of research on mesoscale convective systems. *Meteor. Monogr.* **2018**, *59*, 17–1.
6. Schumacher, R.S.; Rasmussen, K.L. The formation, character and changing nature of mesoscale convective systems. *Nat. Rev. Earth Environ.* **2020**, pp. 1–15.
7. Prein, A.F.; Giangrande, S. Sensitivity of organized convective storms to model grid spacing in current and future climates. Technical report, Brookhaven National Lab.(BNL), Upton, NY (United States), 2020.
8. Prein, A.F.; Liu, C.; Ikeda, K.; Bullock, R.; Rasmussen, R.M.; Holland, G.J.; Clark, M. Simulating North American mesoscale convective systems with a convection-permitting climate model. *Clim. Dyn.* **2017**, pp. 1–16.
9. Gabriel, A.K.; Goldstein, R.M.; Zebker, H.A. Mapping small elevation changes over large areas: Differential radar interferometry. *J. Geophys. Res.* **1989**, *94*, 9183–9191.
10. Massonnet, D.; Feigl, K.L. Radar interferometry and its application to changes in the Earth's surface. *Rev. Geophys.* **1998**, *36*, 441–500.
11. Bürgmann, R.; Rosen, P.A.; Fielding, E.J. Synthetic aperture radar interferometry to measure Earth's surface topography and its deformation. *Annu. Rev. Earth Planet. Sci.* **2000**, *28*, 169–209.
12. Rosen, P.A.; Hensley, S.; Joughin, I.R.; Li, F.K.; Madsen, S.N.; Rodriguez, E.; Goldstein, R.M. Synthetic aperture radar interferometry. *Proceedings of the IEEE* **2000**, *88*, 333–382.
13. Hanssen, R.F.; Weckwerth, T.M.; Zebker, H.A.; Klees, R. High-resolution water vapor mapping from interferometric radar measurements. *Science* **1999**, *283*, 1297–1299.
14. Mateus, P.; Nico, G.; Catalão, J. Can spaceborne SAR interferometry be used to study the temporal evolution of PWV? *Atmos. Res.* **2013**, *119*, 70–80.
15. Chang, L.; Liu, M.; Guo, L.; He, X.; Gao, G. Remote sensing of atmospheric water vapor from synthetic aperture radar interferometry: case studies in Shanghai, China. *J. Appl. Remote Sens.* **2016**, *10*, 046032.
16. Mateus, P.; Catalão, J.; Nico, G. Sentinel-1 interferometric SAR mapping of precipitable water vapor over a country-spanning area. *IEEE Trans. Geosci. Remote Sens.* **2017**, *55*, 2993–2999.
17. Mateus, P.; Catalão, J.; Nico, G.; Benevides, P. Mapping precipitable water vapor time series from Sentinel-1 Interferometric SAR. *IEEE Trans. Geosci. Remote Sens.* **2019**, *58*, 1373–1379.
18. Meroni, A.N.; Montrasio, M.; Venuti, G.; Barindelli, S.; Mascitelli, A.; Manzoni, M.; Monti Guarnieri, A.V.; Gatti, A.; Lagasio, M.; Parodi, A.; others. On the definition of the strategy to obtain absolute InSAR Zenith Total Delay maps for meteorological applications. *Front. Earth Sci.* **2020**, *8*, 359. doi:10.3389/feart.2020.00359.
19. Pichelli, E.; Ferretti, R.; Cimini, D.; Panegrossi, G.; Perissin, D.; Pierdicca, N.; Rocca, F.; Rommen, B. InSAR water vapor data assimilation into mesoscale model MM5: Technique and pilot study. *IEEE J. Sel. Top. Appl. Earth Obs. Remote Sens.* **2015**, *8*, 3859–3875. doi:10.1109/JSTARS.2014.2357685.
20. Mateus, P.; Tomé, R.; Nico, G.; Member, S.; Catalão, J. Three-dimensional variational assimilation of InSAR PWV using the WRFDA model. *IEEE Trans. Geosci. Remote Sens.* **2016**, *54*, 7323–7330. doi:10.1109/TGRS.2016.2599219.
21. Mateus, P.; Miranda, P.; Nico, G.; Catalão, J.; Pinto, P.; Tomé, R. Assimilating InSAR maps of water vapor to improve heavy rainfall forecasts: A case study with two successive storms. *J. Geophys. Res. Atmos.* **2018**, *123*, 3341–3355. doi:10.1002/2017JD027472.
22. Lagasio, M.; Parodi, A.; Pulvirenti, L.; Meroni, A.N.; Boni, G.; Pierdicca, N.; Marzano, F.S.; Luini, L.; Venuti, G.; Realini, E.; others. A synergistic use of a high-resolution numerical weather prediction model and high-resolution Earth observation products to improve precipitation forecast. *Remote Sensing* **2019**, *11*, 2387.
23. Pierdicca, N.; Maiello, I.; Sansosti, E.; Venuti, G.; Barindelli, S.; Ferretti, R.; Gatti, A.; Manzo, M.; Monti-Guarnieri, A.V.; Murgia, F.; others. Excess path delays from Sentinel interferometry to improve weather forecasts. *IEEE J. Sel. Top. Appl. Earth Obs. Remote Sens.* **2020**, *13*, 3213–3228.
24. Oigawa, M.; Tsuda, T.; Seko, H.; Shoji, Y.; Realini, E. Data assimilation experiment of precipitable water vapor observed by a hyper-dense GNSS receiver network using a nested NHM-LETKF system. *Earth Planets Space* **2018**, *70*. doi:10.1186/s40623-018-0851-3.

25. Mascitelli, A.; Federico, S.; Fortunato, M.; Avolio, E.; Torcasio, R.C.; Realini, E.; Mazzoni, A.; Transerici, C.; Crespi, M.; Dietrich, S. Data assimilation of GPS-ZTD into the RAMS model through 3D-Var: preliminary results at the regional scale. *Meas. Sci. Technol.* **2019**, *30*, 055801. doi:10.1088/1361-6501/ab0b87.
26. Hdidou, F.Z.; Mordane, S.; Moll, P.; Mahfouf, J.F.; Erraji, H.; Dahmane, Z. Impact of the variational assimilation of ground-based GNSS zenith total delay into AROME-Morocco model **2020**. *72*, 1–13. doi:10.1080/16000870.2019.1707854.
27. Yang, S.C.; Huang, Z.M.; Huang, C.Y.; Tsai, C.C.; Yeh, T.K. A case study on the impact of ensemble Data Assimilation with GNSS-Zenith Total Delay and radar data on heavy rainfall prediction. *Mon. Weather Rev.* **2020**, *148*, 1075–1098. doi:10.1175/MWR-D-18-0418.1.
28. Hanssen, R.F.; Weckwerth, T.M.; Zebker, H.A.; Klees, R. High-resolution water vapor mapping from interferometric radar measurements **1999**. *283*, 1297–1299.
29. Mateus, P.; Catalão, J.; Nico, G. Sentinel-1 interferometric SAR mapping of precipitable water vapor over a country-spanning area. *IEEE Trans. Geosci. Remote Sens.* **2017**, *55*, 2993–2999. doi:10.1109/TGRS.2017.2658342.
30. Hobbs, S.E.; Guarnieri, A.M.; Broquetas, A.; Calvet, J.C.; Casagli, N.; Chini, M.; Ferretti, R.; Nagler, T.; Pierdicca, N.; Prudhomme, C.; others. G-CLASS: geosynchronous radar for water cycle science–orbit selection and system design. *J. Eng.* **2019**, *2019*, 7534–7537.
31. Cenci, L.; Pulvirenti, L.; Boni, G.; Pierdicca, N. Defining a trade-off between spatial and temporal resolution of a geosynchronous SAR mission for soil moisture monitoring. *Remote Sens.* **2018**, *10*, 1950.
32. Errico, R.M.; Yang, R.; Privé, N.C.; Tai, K.S.; Todling, R.; Sienkiewicz, M.E.; Guo, J. Development and validation of observing-system simulation experiments at NASA's Global Modeling and Assimilation Office. *Q. J. R. Meteor. Soc.* **2013**, *139*, 1162–1178.
33. Privé, N.; Errico, R.; Tai, K.S. The impact of increased frequency of rawinsonde observations on forecast skill investigated with an observing system simulation experiment. *Mon. Weather Rev.* **2014**, *142*, 1823–1834.
34. Hoffman, R.N.; Atlas, R. Future observing system simulation experiments. *Bull. Amer. Meteor. Soc.* **2016**, *97*, 1601–1616. doi:10.1175/BAMS-D-15-00200.1.
35. Sugimoto, S.; Crook, N.A.; Sun, J.; Xiao, Q.; Barker, D.M. An examination of WRF 3DVAR radar data assimilation on its capability in retrieving unobserved variables and forecasting precipitation through observing system simulation experiments. *Mon. Weather Rev.* **2009**, *137*, 4011–4029.
36. Annane, B.; Mcnoldy, B.; Leidner, S.M.; Hoffman, R.; Atlas, R.; Majumdar, S.J. A study of the HWRF analysis and forecast impact of realistically simulated CYGNSS observations assimilated as scalar wind speeds and as VAM wind vectors. *Mon. Weather Rev.* **2018**, *146*, 2221–2236. doi:10.1175/MWR-D-17-0240.1.
37. Cintineo, R.M.; Otkin, J.A.; Jones, T.A.; Koch, S.; Stensrud, D.J. Assimilation of synthetic GOES-R ABI infrared brightness temperatures and WSR-88D radar observations in a high-resolution OSSE. *Mon. Weather Rev.* **2016**, *144*, 3159–3180. doi:10.1175/MWR-D-15-0366.1.
38. Li, Z.; Li, J.; Wang, P.; Lim, A.; Li, J.; Schmit, T.J.; Atlas, R.; Boukabara, S.A.; Hoffman, R.N. Value-added impact of geostationary hyperspectral infrared sounders on local severe storm forecasts-via a quick regional OSSE. *Adv. Atmos. Sci.* **2018**, *35*, 1217–1230. doi:10.1007/s00376-018-8036-3.
39. Parodi, A.; Boni, G.; Ferraris, L.; Siccardi, F.; Pagliara, P.; Trovatore, E.; Foufoula-Georgiou, E.; Kranzlmueller, D. The "perfect storm": From across the Atlantic to the hills of Genoa. *Eos, Transactions American Geophysical Union* **2012**, *93*, 225–226.
40. Sardou, M.; Maouche, S.; Missoum, H. Compilation of historical floods catalog of northwestern Algeria: First step towards an atlas of extreme floods. *Arabian Journal of Geosciences* **2016**, *9*, 455.
41. Diakakis, M.; Deligiannakis, G. Flood fatalities in Greece: 1970–2010. *Journal of Flood Risk Management* **2017**, *10*, 115–123.
42. Llasat, M.; Llasat-Botija, M.; Petrucci, O.; Pasqua, A.; Rosselló, J.; Vinet, F.; Boissier, L. Towards a database on societal impact of Mediterranean floods within the framework of the HYMEX project. *Natural Hazards and Earth System Sciences* **2013**, *13*, 1337.
43. Davolio, S.; Silvestro, F.; Malguzzi, P. Effects of increasing horizontal resolution in a convection-permitting model on flood forecasting: The 2011 dramatic events in Liguria, Italy. *J. Hydromet.* **2015**, *16*, 1843–1856.

44. Nuissier, O.; Ducrocq, V.; Ricard, D.; Lebeaupin, C.; Anquetin, S. A numerical study of three catastrophic precipitating events over southern France. I: Numerical framework and synoptic ingredients. *Q. J. R. Meteor. Soc.* **2008**, *134*, 111–130. doi:10.1002/qj.200.
45. Millán, M.; Estrela, J.; Caselles, V. Torrential precipitations on the Spanish east coast: The role of the Mediterranean sea-surface temperature. *Atmos. Res.* **1995**, *36*, 1–16.
46. Pastor, F.; Gómez, I.; Estrela, M.J. Numerical study of the October 2007 flash flood in the Valencia region (eastern Spain): The role of the orography. *Nat. Hazards Earth Sys. Sci.* **2010**, *10*, 1331–1345. doi:10.5194/nhess-10-1331-2010.
47. Parodi, A.; Ferraris, L.; Gallus, W.; Maugeri, M.; Molini, L.; Siccardi, F.; Boni, G. Ensemble cloud-resolving modelling of a historic back-building mesoscale convective system over Liguria: the San Fruttuoso case of 1915. *Clim. Past.* **2017**.
48. Gallus Jr, W.A.; Parodi, A.; Maugeri, M. Possible impacts of a changing climate on intense Ligurian Sea rainfall events. *International Journal of Climatology* **2018**, *38*, e323–e329.
49. Fiori, E.; Comellas, A.; Molini, L.; Rebora, N.; Siccardi, F.; Gochis, D.; Tanelli, S.; Parodi, A. Analysis and hindcast simulations of an extreme rainfall event in the Mediterranean area: The Genoa 2011 case. *Atmos. Res.* **2014**, *138*, 13–29.
50. Lebeaupin, C.; Ducrocq, V.; Giordani, H. Sensitivity of torrential rain events to the sea surface temperature based on high-resolution numerical forecasts. *J. Geophys. Res. Atmos.* **2006**, *111*.
51. Pastor, F.; Estrela, M.J.; Peñarrocha, D.; Millán, M.M. Torrential rains on the Spanish Mediterranean coast: Modeling the effects of the sea surface temperature. *J. Appl. Meteor.* **2001**, *40*, 1180–1195.
52. Meroni, A.N.; Renault, L.; Parodi, A.; Pasquero, C. Role of the Oceanic Vertical Thermal Structure in the Modulation of Heavy Precipitations Over the Ligurian Sea. *Pure Appl. Geophys.* **2018**, *175*, 4111–4130. doi:10.1007/s00024-018-2002-y.
53. Meroni, A.N.; Parodi, A.; Pasquero, C. Role of SST patterns on surface wind modulation of a heavy midlatitude precipitation event. *J. Geophys. Res. Atmos.* **2018**, *123*, 9081–9096. doi:10.1029/2018JD028276.
54. Cassola, F.; Ferrari, F.; Mazzino, A.; Miglietta, M.M. The role of the sea in the flash floods events over Liguria (northwestern Italy). *Geophys. Res. Letters* **2016**, *43*, 3534–3542. doi:10.1002/2016GL068265.
55. Davolio, S.; Volonté, A.; Manzato, A.; Pucillo, A.; Cicogna, A.; Ferrario, M.E. Mechanisms producing different precipitation patterns over north-eastern Italy: insights from HyMeX-SOP1 and previous events. *Q. J. R. Meteor. Soc.* **2016**. doi:10.1002/qj.2731.
56. Ducrocq, V.; Nuissier, O.; Ricard, D.; Lebeaupin, C.; Thouvenin, T. A numerical study of three catastrophic precipitating events over southern France. II: Mesoscale triggering and stationarity factor. *Q. J. R. Meteor. Soc.* **2008**, *134*, 131–145. doi:10.1002/qj.199.
57. Rudari, R.; Entekhabi, D.; Roth, G. Large-scale atmospheric patterns associated with mesoscale features leading to extreme precipitation events in northwestern Italy **2005**. *28*, 601–614. doi:10.1016/j.advwatres.2004.10.017.
58. Molini, L.; Parodi, A.; Rebora, N.; Craig, G.C. Classifying severe rainfall events over Italy by hydrometeorological and dynamical criteria. *Q. J. R. Meteor. Soc.* **2011**, *137*, 148–154. doi:10.1002/2017JD027472.
59. Dayan, U.; Nissen, K.; Ulbrich, U. Review article: atmospheric conditions inducing extreme precipitation over the eastern and western Mediterranean. *Nat. Hazards Earth Sys. Sci.* **2015**, *15*, 2525–2544. doi:10.5194/nhess-15-2525-2015.
60. Hersbach, H.; Bell, B.; Berrisford, P.; Hirahara, S.; Horányi, A.; Muñoz-Sabater, J.; Nicolas, J.; Peubey, C.; Radu, R.; Schepers, D.; Simmons, A.; Soci, C.; Abdalla, S.; Abellan, X.; Balsamo, G.; Bechtold, P.; Biavati, G.; Bidlot, J.; Bonavita, M.; Chiara, G.D.; Dahlgren, P.; Dee, D.; Diamantakis, M.; Dragani, R.; Flemming, J.; Forbes, R.; Fuentes, M.; Geer, A.; Haimberger, L.; Healy, S.; Hogan, R.J.; Hólm, E.; Janisková, M.; Keeley, S.; Laloyaux, P.; Lopez, P.; Lupu, C.; Radnoti, G.; de Rosnay, P.; Rozum, I.; Vamborg, F.; Villaume, S.; Thépaut, J.N. The ERA5 global reanalysis. *Q. J. R. Meteor. Soc.* **2020**, *146*, 1999–2049. doi:10.1002/qj.3803.
61. Skamarock, W.C.; Klemp, J.B.; Dudhia, J.; Gill, D.O.; Barker, D.M.; Duda, M.; Huang, X.Y.; Wang, W.; Powers, J.G. A description of the Advanced Research WRF Version 3. *NCAR Tech. Note NCAR/TN-475+STR* **2008**, p. 113 pp. doi:10.5065/D68S4MVH.

62. Thompson, G.; Eidhammer, T. A study of aerosol impacts on clouds and precipitation development in a large winter cyclone. *J. Atmos. Sci.* **2014**, *71*, 3636–3658.
63. Hong, S.Y.; Lim, J.O.J. The WRF single-moment 6-class microphysics scheme (WSM6). *J. Korean Meteor. Soc.* **2006b**, *42*, 129–151.
64. European Space Agency. Report for Assessment: Earth Explorer 10 Candidate Mission Hydroterra. *ESA-EOPSM-HYDRO-RP-3779, Noordwijk, The Netherlands* **2020**.
65. Lagasio, M.; Silvestro, F.; Campo, L.; Parodi, A. Predictive capability of a high-resolution hydrometeorological forecasting framework coupling WRF cycling 3dvar and Continuum. *J. Hydrol.* **2019**, *20*, 1307–1377. doi:10.1175/JHM-D-18-0219.1.
66. Lagasio, M.; Pulvirenti, L.; Parodi, A.; Boni, G.; Pierdicca, N.; Venuti, G.; Realini, E.; Tagliaferro, G.; Barindelli, S.; Rommen, B. Effect of the ingestion in the WRF model of different Sentinel-derived and GNSS-derived products: analysis of the forecasts of a high impact weather event. *Eur. J. Remote Sens.* **2019**, *52*, 16–33. doi:10.1080/22797254.2019.1642799.
67. Hong, S.Y.; Noh, Y.; Dudhia, J. A new vertical diffusion package with an explicit treatment of entrainment processes. *Mon. Weather Rev.* **2006**, *134*, 2318–2341.
68. Iacono, M.J.; Delamere, J.S.; Mlawer, E.J.; Shephard, M.W.; Clough, S.A.; Collins, W.D. Radiative forcing by long-lived greenhouse gases: Calculations with the AER radiative transfer models. *J. Geophys. Res. Atmos.* **2008**, *113*.
69. Mlawer, E.J.; Taubman, S.J.; Brown, P.D.; Iacono, M.J.; Clough, S.A. Radiative transfer for inhomogeneous atmospheres: RRTM, a validated correlated-k model for the longwave. *J. Geophys. Res. Atmos.* **1997**, *102*, 16663–16682.
70. Iacono, M.J.; Mlawer, E.J.; Clough, S.A.; Morcrette, J.J. Impact of an improved longwave radiation model, RRTM, on the energy budget and thermodynamic properties of the NCAR community climate model, CCM3. *J. Geophys. Res. Atmos.* **2000**, *105*, 14873–14890.
71. Smirnova, T.G.; Brown, J.M.; Benjamin, S.G. Performance of different soil model configurations in simulating ground surface temperature and surface fluxes. *Mon. Weather Rev.* **1997**, *125*, 1870–1884.
72. Smirnova, T.G.; Brown, J.M.; Benjamin, S.G.; Kim, D. Parameterization of cold season processes in the MAPS land-surface scheme. *J. Geophys. Res.* **2000**, *105*, 4077–4086.
73. Tiedtke, M. A comprehensive mass flux scheme for cumulus parameterization in large-scale models. *Mon. Weather Rev.* **1989**, *117*, 1779–1800. doi:10.1175/1520-0493(1989)117<1779:ACMFSF>2.0.CO;2.
74. Zhang, C.; Wang, Y.; Hamilton, K. Improved representation of boundary layer clouds over the southeast Pacific in ARW-WRF using a modified Tiedtke cumulus parameterization scheme. *Mon. Weather Rev.* **2011**, *139*, 3489–3513.
75. Han, J.; Pan, H.L. Revision of convection and vertical diffusion schemes in the NCEP Global Forecast System. *Weather Forecast.* **2011**, *26*, 520–533. doi:10.1175/WAF-D-10-05038.1.
76. Lagasio, M.; Parodi, A.; Procopio, R.; Rachidi, F.; Fiori, E. Lightning potential index performances in multimicrophysical cloud-resolving simulations of a back-building mesoscale convective system: The Genoa 2014 event. *J. Geophys. Res. Atmos.* **2017**, *122*, 4238–4257. doi:10.1002/2016JD026115.
77. Bevis, M.; Businger, S.; Herring, T.A.; Rocken, C.; Anthes, R.A.; Ware, R.H. GPS Meteorology: Remote sensing of atmospheric water vapor using the Global Positioning System. *J. Geophys. Res.* **1992**, *97*, 15787–15801.
78. Smith, E.K.; Weintraub, S. The constants in the equation for atmospheric refractive index at radio frequencies. *Proc. IRE* **1953**, *41*, 1035–1037.
79. Bevis, M.; Businger, S.; Chiswell, S.; Herring, T.A.; Anthes, R.A.; Rocken, C.; Ware, R.H. GPS Meteorology: Mapping Zenith Wet Delays onto precipitable water. *J. Appl. Meteor.* **1994**, *33*, 379–386.
80. Saastamoinen, J. Contributions to the theory of atmospheric refraction. *Bulletin Géodésique* **1973**, *107*, 13–14.
81. Long, M.W. Radar reflectivity of land and sea. *dchc* **1975**.
82. Zebker, H.A.; Villasenor, J.; others. Decorrelation in interferometric radar echoes. *IEEE Transactions on geoscience and remote sensing* **1992**, *30*, 950–959.
83. Barker, D.; Huang, X.Y.; Liu, Z.; Auligné, T.; Zhang, X.; Rugg, S.; Ajjaji, R.; Bourgeois, A.; Bray, J.; Chen, Y.; others. The Weather Research and Forecasting model's community variational/ensemble data assimilation system: WRFDA. *Bull. Amer. Meteor. Soc.* **2012**, *93*, 831–843.

84. Vendrasco, E.P.; Sun, J.; Herdies, D.L.; Frederico de Angelis, C. Constraining a 3DVAR radar data assimilation system with large-scale analysis to improve short-range precipitation forecasts. *J. Appl. Meteor. Climatol.* **2016**, *55*, 673–690.
85. Tang, X.; Sun, J.; Zhang, Y.; Tong, W. Constraining the large-scale analysis of a regional Rapid-Update-Cycle system for short-term convective precipitation forecasting. *J. Geophys. Res. Atmos.* **2019**, *124*, 6949–6965.
86. Davis, A.C.; Brown, B.; Bullock, R. Object-based verification of precipitation forecasts. Part I: Methodology and application to mesoscale rain areas. *Mon. Weather Rev.* **2006**, *134*, 1772–1784. doi:10.1175/MWR3145.1.
87. Davis, A.C.; Brown, B.; Bullock, R. Object-based verification of precipitation forecasts. Part II: Application to convective rain system. *Mon. Weather Rev.* **2006**, *134*, 1785–1795. doi:10.1175/MWR3146.1.
88. Ebert, E.E. Fuzzy verification of high-resolution gridded forecasts: a review and proposed framework. *Meteor. Appl.* **2008**, *15*, 51–64. doi:10.1002/met.25.
89. Poletti, M.L.; Parodi, A.; Turato, B. Severe hydrometeorological events in Liguria region: calibration and validation of a meteorological indices-based forecasting operational tool. *Meteor. Appl.* **2017**, *24*, 560–570. doi:10.1002/met.1653.
90. Chu, C.M.; Lin, Y.L. Effects of orography on the generation and propagation of mesoscale convective systems in a two-dimensional conditionally unstable flow. *J. Atmos. Sci.* **2000**, *57*, 3817–3837.
91. Chen, S.H.; Lin, Y.L. Effects of moist Froude number and CAPE on a conditionally unstable flow over a mesoscale mountain ridge. *J. Atmos. Sci.* **2005**, *62*, 331–350.
92. Barindelli, S.; Realini, E.; Venuti, G.; Fermi, A.; Gatti, A. Detection of water vapor time variations associated with heavy rain in northern Italy by geodetic and low-cost GNSS receivers. *Earth, Planets and Space* **2018**, *70*, 28. doi:10.1186/s40623-018-0795-7.
93. Radhakrishna, B.; Fabry, F.; Braun, J.J.; van Hove, T. Precipitable water from GPS over the continental United States: Diurnal cycle, intercomparisons with NARR, and link with convective initiation. *JCli* **2015**, *28*, 2584–2599. doi:10.1175/JCLI-D-14-00366.1.
94. Shoji, Y. Retrieval of water vapor inhomogeneity using the Japanese nationwide GPS array and its potential for prediction of convective precipitation. *JMSJ* **2013**, *91*, 43–62. doi:10.2151/jmsj.2013-103.
95. Nahmani, S.; Bock, O.; Guichard, F. Sensitivity of GPS tropospheric estimates to mesoscale convective systems in West Africa. *Atmos. Chem. Phys.* **2019**, *19*.
96. Fink, A.H.; Reiner, A. Spatiotemporal variability of the relation between African easterly waves and West African squall lines in 1998 and 1999. *J. Geophys. Res. Atmos.* **2003**, *108*.
97. Klein, C.; Taylor, C.M. Dry soils can intensify mesoscale convective systems. *Proc. Natl. Acad. Sci. U. S. A.* **2020**, *117*, 21132–21137.
98. Ide, K.; Courtier, P.; Ghil, M.; Lorenc, A.C. Unified notation for data assimilation: Operational, sequential and variational. *J. Meteor. Soc. Jpn.* **1997**, *75*, 181–189.
99. Bouttier, F.; Courtier, P. Data assimilation concepts and methods. Meteorological training course lecture series. *ECMWF. Reading, UK* **1999**.
100. Wang, H.; Huang, X.Y.; Sun, J.; Xu, D.; Zhang, M.; Fan, S.; Zhong, J. Inhomogeneous background error modeling for WRF-Var using the NMC method. *J. Appl. Meteor. Climatol.* **2014**, *53*, 2287–2309. doi:10.1175/JAMC-D-13-0281.1.
101. Sun, J.; Wang, H.; Tong, W.; Zhang, Y.; Lin, C.Y.; Xu, D. Comparison of the impacts of momentum control variables on high-resolution variational data assimilation and precipitation forecasting. *Mon. Weather Rev.* **2016**, *144*, 149–169.